UNIVERSITÀ DEL SALENTO

DEPARTMENT OF MATHEMATICS AND PHYSICS “E. DE GIORGI”
PhD in Physics and Nanoscience

The PADME experiment and the extraction of annihilation cross section

Candidate:
Isabella Oceano

Advisors:
Prof.ssa Stefania Spagnolo
Dott. Gabriele Chiodini

Academic year 2020-2021

Contents

1

Annihilation cross section measurement

The annihilation in two photons is a very important SM candle process for PADME. Gaining a good knowledge of this process allows to monitor with a physics candle the energy scale, the number of positrons hitting the target and detector geometry. In addition, it allows to exercise on a easy test case the strategy to fight the background for the dark search. The signature of this process in the experiment consists in the presence of two photons in the electromagnetic calorimeters. Since the SAC detector is overwhelmed by Bremsstrahlung photons, only the main calorimeter, ECAL, is used to perform this analysis. The goal of this study is to measure the cross section of $e^+e^- \to \gamma\gamma$ using the data collected by the experiment during RunII. In this chapter the entire strategy is described, including a very important and challenging step that is measurement of the efficiency. The technique applied is first described, then validated on dedicated MC samples and applied to data. Nowadays no measurements of the cross section exist at the PADME energy scale. A small review on the two photons annihilation cross section measurement at energies close to $\sqrt{s} =\sim 21$ MeVis given in Appendix ??.

1.1 The cross section measurement strategy

The total cross section, σ_T, for the process $e^+e^- \to \gamma\gamma(\gamma)$ can be measured in PADME using the following relation:

$$\sigma(e^+e^- \to \gamma\gamma) = \frac{N_{sig}}{N_{POT} \times N_{\frac{e}{S}} \times A \times \epsilon} \tag{1.1}$$

where

- N_{sig} is the number of signal processes observed after a selection based on the kinematic correlations typical of annihilation events once subtracted of the background component. In this thesis work several selection procedures for the annihilation process have been considered. In addition to searches based on the identification of a pair of photons, event selection using only one photon have been studied. The choice among the various possibilities has been taken balancing the difficulty in estimating the background from physics process and from spurious beam interaction and the difficulty in evaluating the overall selection efficiency;

- N_{POT} is the total number of positrons hitting the target measured with the active Diamond target;
- $N_{\frac{e}{S}}$ is the number of atomic electrons per unit surface in the PADME target. It is estimated as $N_{\frac{e}{S}} = \frac{\rho \times N_A \times Z \times d}{M_w} = 0,0105\ \mathrm{b}^{-1}$, where $\rho = 3,52\ \mathrm{g/cm}^3$ is the Diamond density, N_A is the Avogadro number, Z the atomic number, $d = 100\ \mu\mathrm{m}$ is the target thickness and M_w is the atomic weigh;
- A is the acceptance of the PADME detector and of the selection criteria applied. Therefore, it results from both geometric and kinematic constraints. The determination of the acceptance will be describen in Section 1.5.1. The acceptance allows to relate the total cross section σ_T to the so called fiducial cross section σ_F, corresponding to the fraction of the cross section directly visible in the experimental apparatus and lying within the kinematic selection requirements $\sigma_T = \sigma_F / A$;
- ϵ is the overall efficiency to identify signal processes. It represents the combination of the detection efficiency of the PADME calorimeter. the photon reconstruction and identification efficiency for both photons and the event selection efficiency. Therefore, when N_{sig} is measured with a selection requiring two photons in ECAL, the efficiency ϵ is the product of the identification efficiencies, $\epsilon(\gamma_1)$ and $\epsilon(\gamma_2)$ of the two photons.

Detector defects and asymmetries often prevent the performance of photon reconstruction algorithms to be uniform. Therefore, the event efficiency varies depending on the regions of the detector where the photons have been detected and, in general, the efficiency ϵ cannot be applied as a constant term in Eq. 1.1, unless it is estimated as an average value over the data sample.

Several procedures can be applied to generalize 1.1 taking into account these problems. An approach consists in measuring the fiducial cross section as follows:

$$\sigma_F = \sigma(\theta_0 < \theta_{\gamma_{1,2}} < \theta_1) = \frac{\sum W_i - N_{bkg}}{N_{POT} \cdot n_{\frac{e}{S}}} \tag{1.2}$$

Each candidate contributes to the counting with a weight accounting for all the efficiency factors that determine the probability of such event to be selected. N_{bkg} is the estimated background contaminating the sample of selected events. For the candidate annihilation event i, the weight W_i is given by the inverse probability to identify the two photons in the event:

$$W_i = P^{-1}(\theta_{\gamma_{i_1}}, \theta_{\gamma_{i_2}}) = [A_{eff}(\theta_{\gamma_{i_1}}, \theta_{\gamma_{i_2}}) \times \epsilon(\theta_{i_1}, \phi_{i_1}) \times \epsilon(\theta_{i_2}, \phi_{i_2})]^{-1} \tag{1.3}$$

where $\epsilon(\theta_{i_{1,2}}, \phi_{i_{1,2}})$ is the efficiency as a function of the position in the calorimeter for the first or second photon. The factor $A_{eff}(\theta_{\gamma_{i_1}}, \theta_{\gamma_{i_2}})$ is the visible acceptance and it represents a correction to the acceptance that takes into account resolution effects causing the migration of events from the acceptance region to the outside and vice versa. It will be discusses in more details and estimated in Section 1.5.2.

The efficiency values used in Eq. 1.2 can be estimated with simulation or can be directly measured in data if a suitable sample of reference photons can be defined and used to measure the fraction of them that is successfully detected and identified. Section reference describes that data-driven determination of the efficiency that is used in the cross section measurement, exploiting the approach of Eq. 1.2.

Data-driven efficiency measurements may be affected by biases. On the other hand, simulations are often affected by residual mismodeling of the detector response and geometry and of the beam features. Another strategy, meant to address these problems, consists in estimating the reconstruction and selection efficiency in a simulation corrected for data mismodeling. In practice, this is done by replacing ϵ in Equation 1.1 with a global efficiency factor C corresponding to the ratio of simulated to generated events inside the fiducial requirements corrected for mismodelling. The corrections are defined in terms of scale factors equal to the ratio between the event dependent efficiency measured in data $\epsilon^{data}(\theta, \phi)$ and in simulation $\epsilon^{MC}(\theta, \phi)$, the latter being obtained with exactly the same method applied in the case of data. In summary,

$$\sigma_F = \frac{N_{sel}}{C \cdot N_{POT} \cdot n_{\frac{e}{S}}}, \tag{1.4}$$

$$C_{\gamma\gamma} = \frac{N_W^{MC,gen}(\theta_{min} < \theta_{\gamma_1,\gamma_2} < \theta_{max})}{N^{gen}(\theta_{min} < \theta_{\gamma_1,\gamma_2} < \theta_{max})}, \tag{1.5}$$

$$N_W^{MC,gen}(\theta_{min} < \theta_{\gamma_1,\gamma_2} < \theta_{max}) = \sum_i f_i^{data/MC}, \tag{1.6}$$

$$f_i^{data/MC} = \prod_j f_{i,j}^{data/MC} \tag{1.7}$$

where $f_{ij}^{data/MC}$ is the data-simulation scale factor for any efficiency contribution, for example the efficiency for photon 1 in event i leads to a scale factor $f_{i1} = \epsilon_{DD}^{data}(\theta_1, \phi_1)/\epsilon_{DD}^{MC}(\theta_1, \phi_1)$, where the efficiency $\epsilon_{DD}^{data}(\theta_1, \phi_1)$ is measured with a data driven (DD) method both in data and in Monte Carlo. The quantity N_W^{MC} therefore represents the number of signal events selected in the simulation, but corrected for local mismodelling of data, and N^{gen} is the number of simulated signal events that at generator level fall in within the acceptance of the selection. Finally, the factor C would correspond to purely MC based efficiency for the selection if all scale factors were equal to 1.

In this work the cross section measurement will be derived using Equation 1.1, and Equation 1.2 as a cross check, relying on a data-driven determination of the photon selection efficiency. The possible biases of the methods are studied in dedicated simulations and found to be negligible or mitigated by compensation effects. This topic will be discussed in Section reference where the cancellation due to compensation effects will be described and in Section reference where a careful implementation of the data driven method will be shown to leave no sign of biases.

The second approach based on scale factors was also investigated and found to be a powerful methodology to validate the strategy for the data-driven efficiency measurement. However, it was not used for the measurement due to the unavailability of suitable simulation of the PADME beam line.

1.2 Theory prediction

1.3 Data sample, simulation and reconstruction

1.3.1 Data sample

The data used for this measurement have been chosen among the sample collected during RunII, because of the smallest background level, as seen in Chapter data taking. During this run the energy of the beam was $E_{beam} = 430$ MeV and the beam density ~ 100 POT/ns. A summary of the runs used for the analysis with their main features is collected in Table 1.1. The total number of positrons on target corresponding to the sample is $N_{POT}^{tot} = 3,97 \times 10^{11}$. In Figure 1.1 structure in time of the bunch is shown. As highlighted by Table and Figure the runs have different features not only in multiplicity per bunch but also in bunch structure, meaning that the runs are collected with different beam configurations. This selection of runs was chosen because of a good stability of the beam intensity in time within the each run. Indeed a data quality monitor processing of the data shows that the number of positrons on target measured by the Diamond is very stable as is shown in Figure 1.2 for run $N = 30617$.

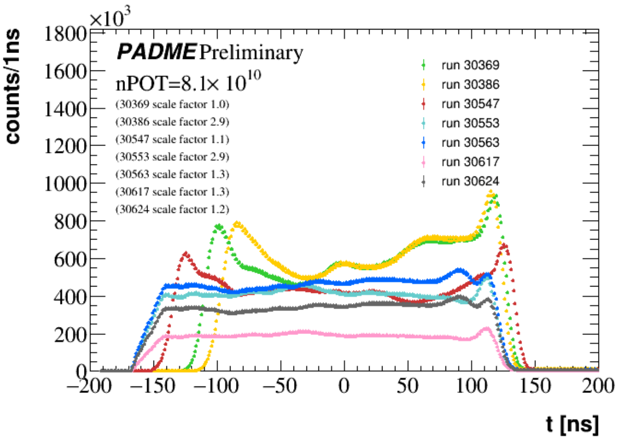

Figure 1.1: *Bunch structure for each run analysed recorded with SAC.*

A special data sample consisting of two runs, recorded with the target out of the beam line, has also been used. This sample allows to study the beam related background observed in PADME .

With a total of $N_{POT} = 4 \times 10^{11}$, assuming a product of acceptance and efficiency of the order of $\sim 5\%$ the number of detected annihilation events is about ~ 521000; if background was negligible or compatible with the signal, the relative statistical error on the cross section measurement would be $\sim 1\%$ and even if the background rate was ten times larger than

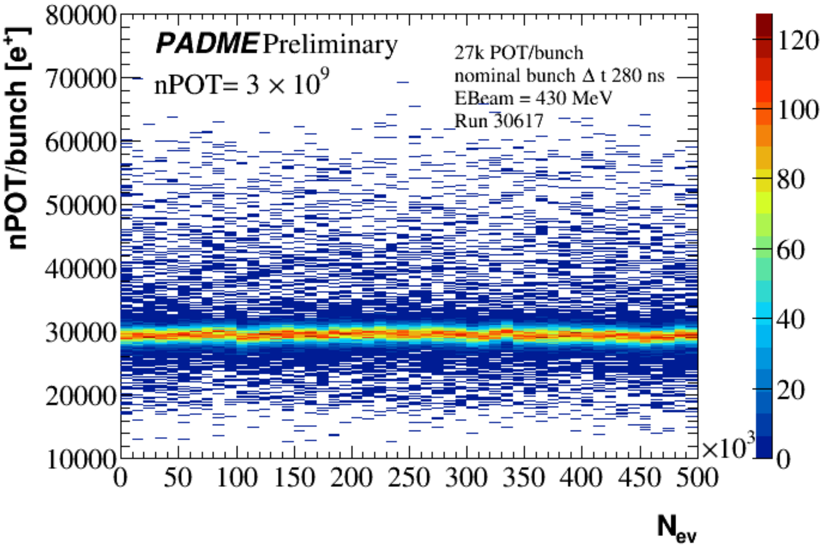

Figure 1.2: *Number of positrons per bunch as a function of the event number for run* 30617.

Table 1.1: *Main features of the analysed runs: run number, total N_{POT} measured by target, mean and sigma of a gaussian fit to the peak of the N_{POT} distribution, bunch length and month of data taking.*

Run number	$N_{POT}/10^{10}$	$\mu(N_{POT})$	$\sigma(N_{POT})$	bunch length [ns]	Date	
30369	$8,2$	26993	1738	260	Sept	
30386	$2,8$	19057	1385	240	Sept	
30547	$7,1$	31480	1402	270	Oct.	
30553	$2,8$	35729	1314	260	Oct.	
30563	$6,0$	26785	1231	270	Oct.	
30617	$6,1$	27380	1496	270	Nov.	
30624	$6,6$	29515	2070	270	Nov.	
30654	/	~ 27000	/	~ 270	Nov.	no target
30662	/	~ 27000	/	~ 270	Nov.	no target

the signal, the statistical uncertainty would be $\leq 1\%$ which is unlikely to be larger than the systematic uncertainties affecting the measurement. Therefore the sample selected is adequate in size to the measurement.

1.3.2 Simulation samples

The PADME MC is based on a GEANT4 [?] simulation of the experimental apparatus and of the beam. Annihilation processes are simulated when the positrons of the beam cross the Diamond target along with the other dominant QED processes: Bremsstrahlung in particular, Bhabha scattering, and others minor effects. However, similarly to what happens in PADME, a large number of positrons per bunch must be simulated in order to achieve a reasonable statistics of annihilation processes, therefore the final state from a $e^+e^- \rightarrow \gamma\gamma$ event often overlaps with other photons in the the calorimeter, and moreover, the signal photons are not labelled to be easily distinguished. In order to study the kinematics of annihilation events either in a background free simulation, or flagging the final state particles, the CalcHEP generator was used. From the $e^+e^- \rightarrow \gamma\gamma$ generation, a text file was saved with the four-momenta of all particles involved in the process. A special functionality in PADMEMC allows to plug the two photons from an event generated by CALCHEP in a point of the target where a positron from the incoming beam is killed. The photons are then propagated through the detectors like any particle managed by GEANT4.

Several MC data samples were used across the analysis:

1. CalcHEP event generator samples, used to study the MC truth and generator level properties;

2. CalcHEP samples simulated with PADMEMC with a beam consisting of a single positron. In this case the final state of each event contains only two photons from e^+e^- annihilation that can fall inside or outside the detector geometrical acceptance;

3. CalcHEP samples simulated with PADMEMC as in case two but with a beam of 25×10^3 positrons in average in a bunch. This kind of simulation allows to investigate the effect of pileup of the signal event with physics background processes originated from beam interactions in the target.

The CalcHEP generator performs all calculations in the LO approximation for the final state selected by the user, that can be in our case, $\gamma\gamma$ or $\gamma\gamma\gamma$. The same techniques was used to plug annihilation events generated by Babayaga at the NLO approximation in the PADME MC. Therefore a Babayaga generation output at LO was used to check the consistency with CalcHEP and another generation at NLO was used to evaluate the acceptance of the annihilation.

1.3.3 Event reconstruction

The selection of annihilation events uses only the PADME BGO electromagnetic calorimeter. Therefore, here a brief reminder of the main features of the reconstruction of clusters in ECAL is given, while an extensive description of the algorithms is given in Chapter reference.

The multi hit reconstruction, described in Chapter ?? Section ??, was used. For each waveform up to three hits can be identified, with energy and time estimated with a fit with a signal template obtained from clean waveforms recorded in a single positron run. The template allows to naturally account and correct for problems related to the data acquisition like the limited acquisition time window and the saturation. For signals where only one hit is identified in the waveform, energy and time determination follow the same logic applied in the single hit reconstruction, described in Chapter ?? Section ??.

Once the hit collection is defined, clusters are reconstructed merging hits in nearby crystals in time coincidence. The energy required for the cluster seed is 20 MeV, while hits contributing to the cluster must have energy above 1 MeV, a distance from the seed not exceeding three crystals, and a maximum distance in time from the seed of 6 ns.

The cross section measurement requires the determination of the number of POT. This was estimated using the calibration procedure described in Section verify that in padme chapter there is the description. This procedures rely on the absolute energy calibration of the BTF calorimeter that is verified to 5%. The systematic uncertainty on the N_{POT} measurement arises from the calibration procedure, and can be assessed by studying the stability and consistency with the energy seen in other detectors, in particular in the SAC, that collects all forward Bremsstrahlung photons produced by interactions of the beam in the target.

1.4 Experimental signature of annihilation events

The selection of annihilation processes is based on the constrained photon-photon kinematics. In the assumption of a final state consisting of exactly two photons sharing the energy and momentum of the initial state, several relationships between the energies E_1 and E_2, the polar angles[1] θ_1, θ_2, and the azimuthal angles[2] ϕ_1, ϕ_2 of the photons, can be exploited. The most relevant of them are listed in the following, adopting the convention of using the the index 1 for the most energetic photon in the pair:

1. the sum of the energies E_1+E_2 is equal to the beam energy with very good approximation;
2. the transverse momenta of the photons are back to back, therefore $\phi_1 + \pi = \phi_2$
3. for each photon the polar angle θ is a function of the energy;
4. As a consequence of properties 1 and 3 the polar angle of the two photons are strictly correlated;
5. The previous considerations also imply that knowing E_1 sets the value the polar angle of the second photon θ_2; the same is true if the role of the two photons is exchanged;
6. The momentum balance implies also the following relation between the coordinates of the impact point of the two photons in a transverse plane

$$x(y)_{CoG} = \frac{x(y)_1 E_1 + x(y)_2 E_2}{E_1 + E_2} \sim 0. \tag{1.8}$$

In Figure 1.3 the correlation between the energy and the polar angle θ of the two photons is reported along with the two photons energy correlation and the distance in ϕ between a photon and the other extrapolated in the backward direction. Figure 1.4 shows the X and Y center of gravity for a sample specify sample used are also reported.

---

[1] The polar angle θ is defined as the angle between the photon direction and the z axis of the PADME reference frame, which is assumed to match the direction of the incoming positron beam.

[2] The azimuthal angle ϕ is the angle between the direction of a photon in the plane perpendicular to the beam and a reference axis conventionally chosen to be the x axis.

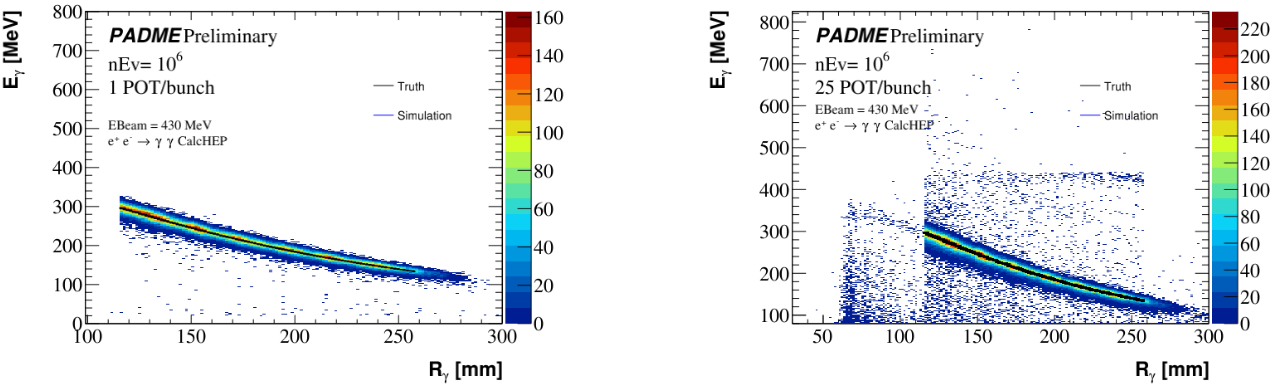

(a) (b)

Figure 1.3: *Correlation between energy and radius of the photon for pure annihilation simulation (a) and adding pileup (b).*

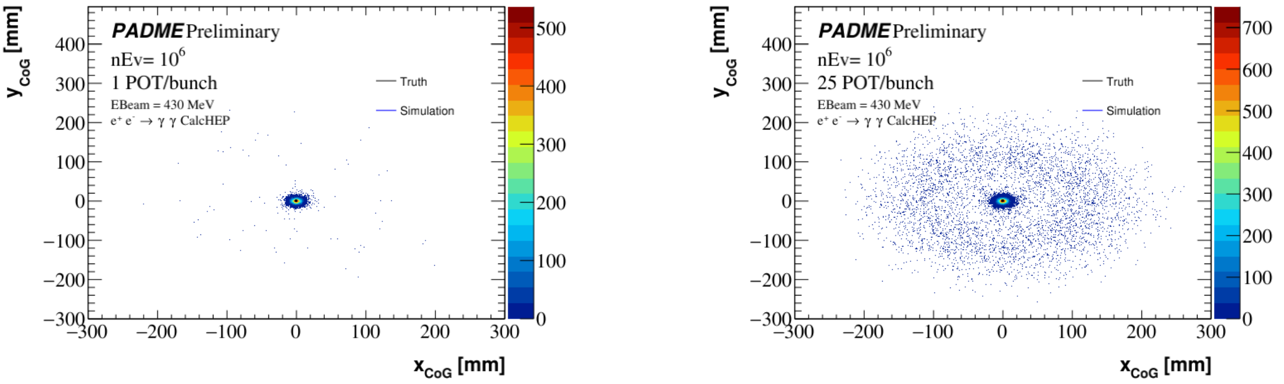

(a) (b)

Figure 1.4: *X and Y CoG map for pure annihilation simulation (a) and adding pileup (b).*

When the beam intensity is of the order of $25k$ POT/bunch, the pair of photons in time coincidence produced by an annihilation event is overlapped to energy deposits in the calorimeters and hits in the veto detectors that are produced by the physics background processes due to interactions of other positrons in the bunch with the target. The background photons, positrons and possibly electrons seen in the detectors are distributed within the 250 ns time width of the bunch. Therefore, the time coincidence between the two signal photons is a powerful handle to suppress the background which can be used along with the kinematic correlations. Fig. xx, yy, zz ask show the distributions of the same variables shown in Fig. xx-nopileup - zz-nopileup for a sample of annihilation events generated with calchep and simulated in PADMEMC along with 25000 positrons.

In the PADME data the pictures is complicated by the beam induced background, which due to the high rate imply a high probability of accidental two-photon coincidence, and in general accidental occurrence of the kinematic correlations typical of annihilation events.

The annihilation yield, i.e. the number of annihilation processes seen in the PADME detector, can be measured starting from the distribution of the sum of the two photon energies, from the CoG distributions or from the difference in the azimuthal angle $\Delta\phi = \phi_1 + 180^\circ - \phi_2$. In all these distributions a peak corresponding to the signal events will emerge over the combinatorial background, if the other correlations are used to select the signal and suppress the background, provided the background rate is below a certain level. Additional selection criteria efficient for the signal consist in setting a minimum photon energy threshold and requiring that the photon has an energy close to the value compatible with its polar angle: $|\Delta E| = |E_\gamma - E(\theta_\gamma)| < \Delta_E^{Max}$.

In the following a sequence of selection cuts, summarized in Table 1.2, will be used to show how the annihilation signal emerges in RunII data.

Table 1.2: *Annihilation selection cut, threshold applied on each variables and cut flow for CalcHEP simulation with pileup from* 25000 *positrons per bunch and for data (run 30563).*

Cut description		Threshold	Simulation	data
Time coincidence	$\|t_{\gamma_1} - t_{\gamma_2}\|$	< 10 ns		
γ_1 in FR	R_{γ_1}	$\in]115.82 \text{ mm}, 258 \text{ mm}[$	$0,70$	$0,73$
CoG	$\|x_{CoG}\|$	< 50 mm	$1,00$	$0,87$
CoG	$\|y_{CoG}\|$	< 50 mm	$1,00$	$0,96$
γ energy	$E_{\gamma_1}, E_{\gamma_2}$	$\in [90 \text{ MeV}, 400 \text{ MeV}]$	$1,00$	$1,00$
sum of γ energies	$E_{\gamma_1} + E_{\gamma_2}$	$\in [300 \text{ MeV}, 600 \text{ MeV}]$	1.00	$0,98$
γ_2 in FR	R_{γ_2}	$\in]115.82 \text{ mm}, 258 \text{ mm}[$	$0,96$	$0,96$

Where the energy thresholds are defined studying the CalcHEP truth, see Figure 1.5.

Ci vuole un plot di Delta T nei dati la selezione di fig 1,3 per esempio, ovviamente senza taglio in Dt e con |COG|<50 + commento Ci vuole un plot di Delta Phi nei dati la selezione di fig 1,3 per esempio, ovviamente senza taglio in DPhi e con |COG|<50 + commento In addition to the cuts on the kinematic variables and on the time coincidence, a geometrical requirement is introduced to ensure a reliable reconstruction of the photons. Indeed, the position of the clusters in ECAL must be at distance from the inner and from the outer border of the calorimeter equal to al least twice the width of a BGO crystal. This ensures limited shower leakage and therefore a good determination of the energy and position. Adding in sequence selection cuts improves the background rejection as demonstrated by Figure 1.7 where the sum of the energy of the two selected photons $E_{\gamma_1} + E_{\gamma_2}$ is shown the red distribution corresponds to events passing the time coincidence and the fiducial region requirement for the most energetic photon γ_1. The amount of background is strongly reduced adding the CoG request (blue distribution). The energy cuts applied to each photon help to further reduce the background. The population of events under the peak, clearly corresponding to annihilation processes, is not significantly reduced by the cuts.

Figure 1.8 (a) shows that the additional cut of the FR on the second photon (the less energetic one) reduces (of $\sim 5\%$) the yield of the annihilation. In Figure 1.8 (b) only the most

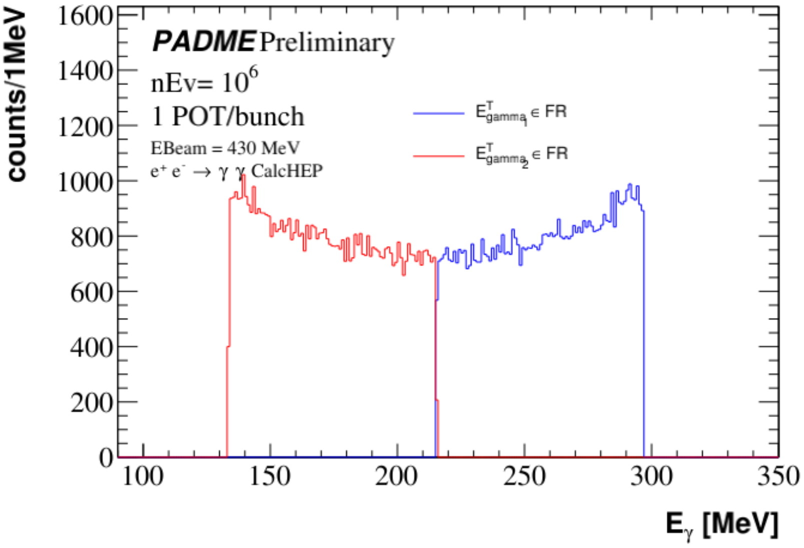

Figure 1.5: *Photon energy distributions in blue for the first photon (in energy) and in red for the second photon.*

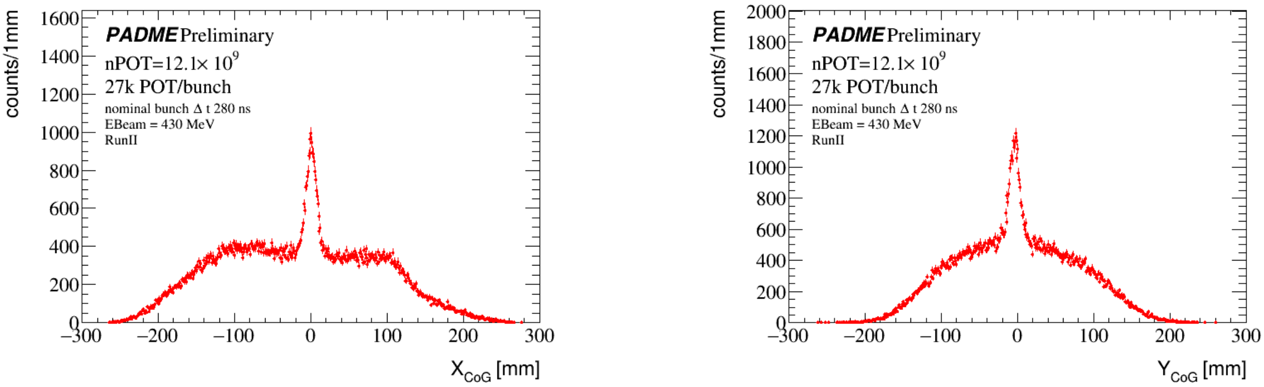

(a) **(b)**

Figure 1.6: *Distribution of the Center Of Gravity variables for the events that satisfy the following cuts, described in Table 1.2: time coincidence and first photon in FR. On the left (a) the distribution of* X_{CoG}*, on the right (b) the distribution of the* Y_{CoG}*.*

energetic photon is required to be in the FR. It's interesting to notice that, because of the cut in the inner radius for the leading photon, E_{γ_1} is contrained to be > 100 MeV, on the other hand the energy of the second photon is not subject to sharp cuts, and ranges from about 50 MeV up to 300 MeV. Most of the studies performed are done with two analysis variant: selecting only events with the first photon in the FR or selecting events with both photons in the FR.

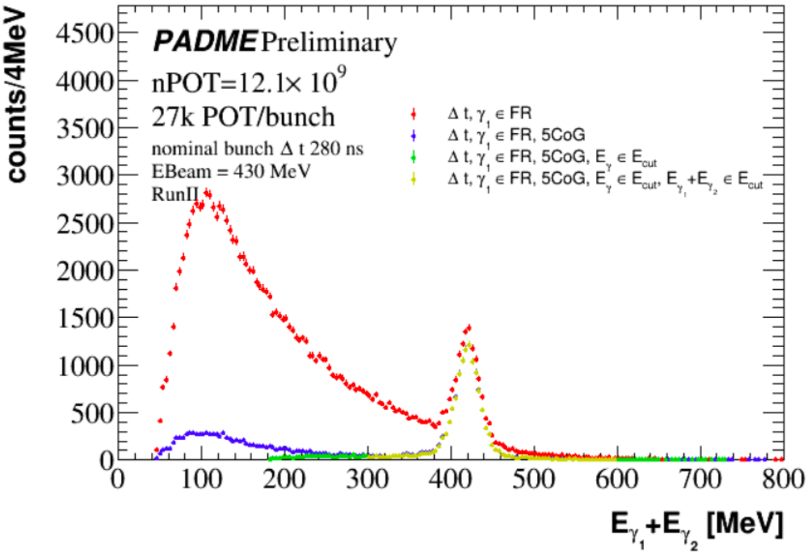

Figure 1.7: *Distribution of $E_{\gamma 1} + E_{\gamma 2}$ for pairs of photons passing various sets of cuts. In red events that pass the time coincidence request with the first photon in the FR; in blue the distribution for events passing also the CoG cut* (5 cm)*. Finally in green (yellow) events satisfy also the energy requirements for one photon (both photons).*

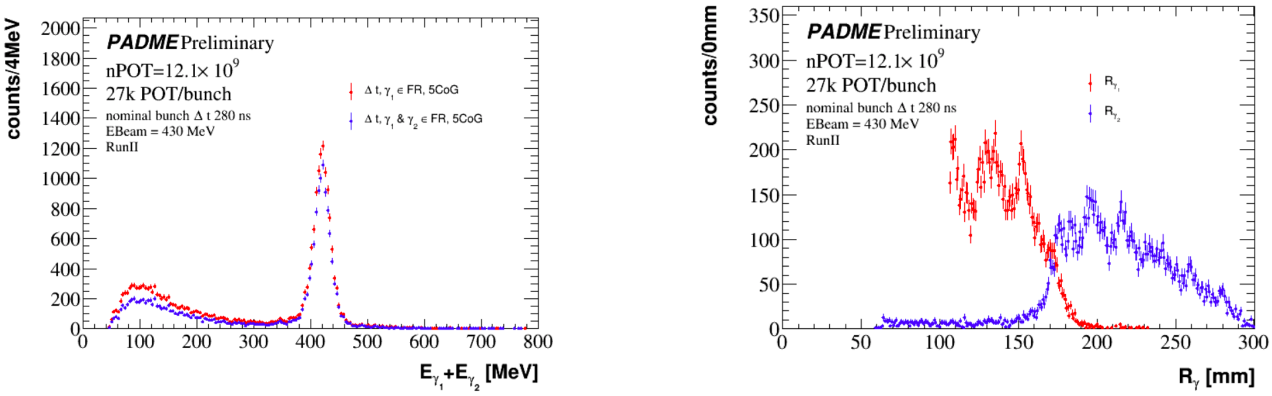

(a) (b)

Figure 1.8: *(a) Distribution of the sum of $E_{\gamma 1} + E_{\gamma 2}$ for the events that pass the cuts on time coincidence and CoG. In red the request of FR is applied only to the most energetic photon, while in blue on both photons. (b) Radius distribution for the most energetic photon γ_1 in red and for the less energetic one γ_2 in blue for the events that pass the time coincidence, FR on the most energetic photon, CoG, energetic cuts.*

1.5 Acceptance

The acceptance has been introduced in Equation 1.1 as a global factor describing the fraction of events corresponding to the process under study that can be detected with the experimental apparatus of PADME and the kinematic requirements applied in the event selection procedure. This concept is based on the assumption of full efficiency of the PADME detectors, DAQ and data reconstruction algorithms. Indeed, in Equation 1.1 all the motivations that can lead to a loss of signal in the data of PADME related to instrumental effects are described through the efficiency term ϵ. As a consequence, the determination of the acceptance must be based on a generator-level simulation of the signal process, before any efficiency, resolution, miscalibration effect plays any role.

The selection cuts described in Table 1.2 are all applied to kinematic properties, involving energies and momenta, except for the requirement that the most energetic photon (or both photons) fall inside a fiducial region of the electromagnetic calorimeter described by an inner and an outer radius. This cut, apparently defined as a geometrical criterion, is dictated by the ECAL geometry but it also has an impact on the energy distribution of the signal photons due to the completely closed kinematics of the two-photon final state in a e^+e^- annihilation process. This requirement is also the only selection cut shaping the phase space of the annihilation process. Indeed, all other cuts are dictated by considerations related to the detector and reconstruction resolution. In summary, if PADME would measure with infinite resolution the photon energies, and positions, each of the selection cut, except for the FR requirement, would have no effect on any signal event with exactly two photons.Therefore, the assessment of the acceptance is strictly related to the definition of the boundaries of the fiducial region.

These boundaries need to be set inside the geometrical boundaries if the calorimeter in order to minimize the effect of the shower leakage. In addition the strong correlation of the two photons implies that for a given value of the beam energy, setting a constraint on the region where, for example, the most energetic photon can be found, directly defines the corresponding region where the second most energetic photon can lie. In order to choose a consistent definition of the fiducial region and estimate the corresponding acceptance a dedicated study was done using CALCHEP and Babayaga simulations at generator level or simulated with a single positron per bunch.

The CalcHEP generator has been used to produce a sample of 10^6 annihilation events according to the LO approximation for the process $e^+e^- \to \gamma\gamma$, with an electron momentum $\vec{P_{e^-}} \sim 0$ MeV/c and a positron energy equal to the energy of the beam $E_{e^+} = 430$ MeV. The three components of the momenta $\vec{P}$ of the two photons of the final state are saved on a text file and used directly to study the events before any detector effect. The same events simulated in PADMEMC allow to assess detector and resolutions effects.The truth information can easily be compared with the simulated event.

A crucial quantity is the radial distance from the original beam direction of the cluster produced by the photon in the calorimeter. In data and in simulation this quantity is computed from the energy weighed position of the BGO crystals in the cluster (see Section reconstruction.. for a detailed discussion).

The measured R_γ allows to measure the polar angle of the photon through the relation

$$R_\gamma = tan(\theta) \times D = \frac{p_T}{p_z} \times D \tag{1.9}$$

where p_T and p_z are the transverse ad longitudinal components of the photon momentum and

D is the distance between the target and the plane perpendicular to the z axis representing the ECAL measurement plane.

The parameter D does not match the distance between the target and the entrance surface of the crystals in ECAL. The position of the target and of the ECAL calorimeter in the PADME reference framework are known from design and from survey measurement. The first is $z_{Target} =$ 1030 mm and, due to the fact that the thickness of the target is very small it is also considered as the distance of the annihilation production point and the origin of the z axis of PADME that is defined as the center on the dipole magnet. Concerning the z coordinate of ECAL, there are three options to consider: the ECAL front face, the plane where the shower reaches the maximum development and the one corresponding to the mean multiplicity of charged particles in the shower. In Figure 1.9 the distribution of the z coordinates of the GEANT4 hits produced by charged particles in the electromagnetic shower is shown. Thus the options for the coordinate of the ECAL measurement plane are:

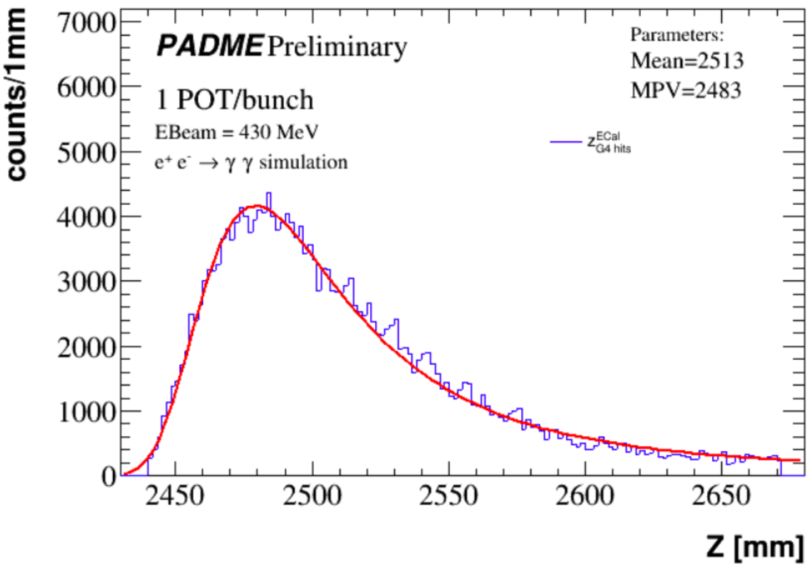

Figure 1.9: *Distribution of the z coordinate of all the hits generated in the BGO crystals of ECal superimposed by a fit using a landau function. The simulation used CalcHEP events simulated in PADMEMC.*

- target - ECAL front face, equal to 2440 mm;
- target - most probable value of the shower maximum, equal to 2483 mm, obtained from a fit of the shower longitudinal profile with a landau function;
- target - mean of the shower profile, equal to 2513 mm.

The value of the distance $D = 1030 + 2513$ mm using the mean of the shower z profile if finally chosen. This value statistically guarantees a good match between the radius R_γ computed from the true photon directly with Equation 1.9 and the R_γ corresponding to the cluster position in the simulation. The distributions of the differences between $R_{truth}(3543 \text{ mm})$ and $R_{cluster}$ for the most energetic photon and the least energetic one are shown in Figure 1.10 right and left respectively. Both the distributions, for this value of D, have the mean of the gaussian fit close to 0 and a standard deviation of $\sim$ 5 mm.

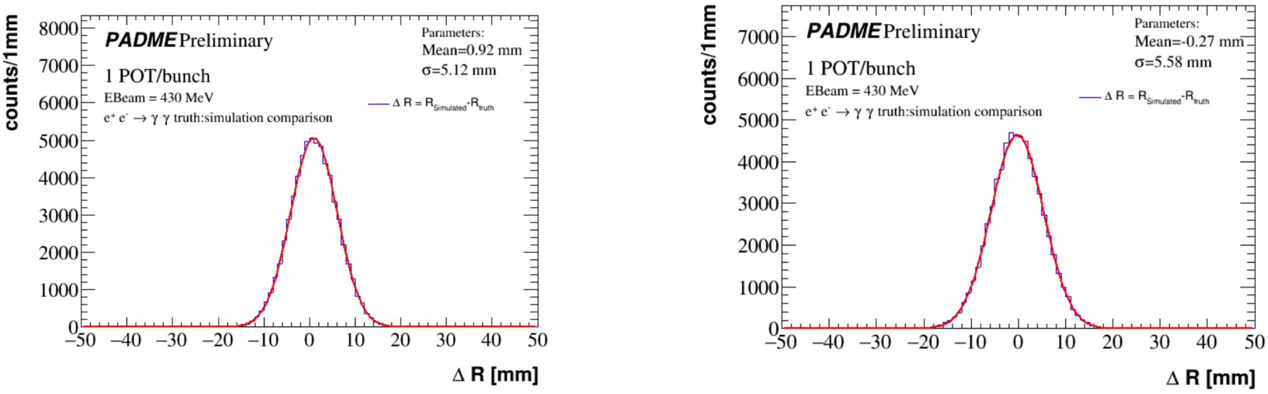

(a) **(b)**

Figure 1.10: *Distribution of the difference between the radius of the photon simulated in PADMEMC and the radius of the truth in the plane at a distance* $D = 3543$ mm *from the diamond target for the most energetic photon (a) and for the second energetic photon (b).*

Clusters in ECAL may be used as photon candidates if the measured energy and position are reliable. For photons hitting the calorimeter in a peripheral regions, energy and positions are likely biased. The features of the clusterization algorithm implemented in the reconstruction suggest that the bias due to transversal shower leakage is small if the cluster position (computed as the energy weighted position of the crystals contributing to the cluster, that must be at a distance from the seed of no more than two crystals) is reconstructed at a distance at least equal to twice the pitch of the BGO crystal matrix. Using this criterion, the maximum radius of a reliable cluster is equal to 258 mm. Due to the fact that the first and the second photon are correlated in energy, thus in space, the corresponding minimum radius is constrained by the kinematics. In practice it is extracted with a scan on R_{min} studying the number of γ_1 and γ_2 with radius inside the range according to MC truth in a CALCHEP $e^+e^- \to \gamma\gamma$ sample. The value of R_{min} that gives a number of first (most energetic) photons equal to the number of second photon is chosen. As a result the fiducial region for the selection of annihilation photons in the PADME calorimeter is defined as the interval $FR = [115.82, 258]$ mm. Another important parameter is the value of the radius $R_{mid} = R_{\gamma_1}(E_{mid}) = R_{\gamma_2}(E_{mid})$ where the two photons have the same energy and therefore the same radius. This parameter, for an energy of the beam $E_{beam} = 430$ MeV, is equal to $R_{mid} = 172.83$ mm. Table 1.3 reports the number of γ_1 and γ_2 ($N_{\gamma_{1(2)}}$) found in ECAL regions defined in terms of the parameters R_{min}, R_{max} and R_{mid}. The counters shows the consistency of the definition for the three parameters, since the number of N_{γ_1} is equal to N_{γ_2}, and all the most energetic photons fall in the inner ring of

ECAL while all those with a lower energy fall in the outer ring as expected by kinematics. In addition in Table 1.3 the number of photons in the upper and lower ECAL region are reported. This number show as for each γ_1 correspond a γ_2 in the opposite ECAL region (e.g. all the γ_1 belonging to the inner ring of ECAL and the upper region have a corresponding γ_2 in the outer ring in the lower region of ECAL).

Table 1.3: *Yield of the most energetic photon* γ_1 *and the less energetic one* γ_2 *in the ECAL regions. The radius range* $]115.82, 258[$ mm *is considered be the fiducial region, the radius* $R_{mid} = 172.83$ mm *is the radius where the two photon has the same energy. The counters are reported also for the upper and lower parts of the detector.*

Cuts	N_{γ_1}	N_{γ_2}
$\gamma \in]115.82, 258[$ mm	65320	65318
$\gamma \in]115.82, 172, 83[$ mm	65320	0
$\gamma \in [172, 83, 258[$ mm	0	65318

A confirmation that the distance target-ECAL considered is the appropriated, is given by the fact that the the same value for R_{mid} is determined by applying the same considerations to the CALCHEP sample simulated in PADMEMC. Figure 1.11 shows the distribution of R_γ for the first (most energetic) and the second photon. Two selections of events are represented: the first defined by the request that $R^T_{\gamma_1}$, i.e. the true radius of the first photon is in the FR (i.e. in the range R_{min}, R_{max}); the second defined by the request that $R^R_{\gamma_1}$, i.e. the radius of the first photon as reconstructed in simulation is in the FR. For the first case the distribution of $R^T_{\gamma_1}$ and $R^T_{\gamma_2}$ are shown in blue by the solid and dotted line respectively. The two distributions do not overlap and span the entire range of the FR with the first (second) photon well contained below (above) R_{mid}. For the second selection, the distributions of $R^R_{\gamma_1}$ and $R^R_{\gamma_2}$ are shown by the green solid and dotted line respectively. As expected, the distribution of $R^R_{\gamma_1}$ is sharply defined at R_{min}, but some migration above R_{mid} is induced by resolution; similarly, the corresponding $R^R_{\gamma_2}$ distribution starts before R_{mid} and ends after R_{max}. Finally, for the second selection the distributions of $R^T_{\gamma_1}$ and $R^T_{\gamma_2}$ are shown by the cyan histograms with solid and dotted line respectively, showing migration of events at the edges of the FR due to resolution.

The same correlation between the radius of the first and second photon predicted by the simulation should be observed if beam energy and detector geometry are well known. In Figure 1.12 the points show R_{γ_2} as a function of R_{γ_1} in PADME annihilation events. The annihilation photon candidates are selected with the application of the cuts presented in the Section 1.4 (in particular cuts a,b,c,d,e are applied). The black continuous line is correlation between observed in CalcHEP sample using MC truth. The agreement is a check of the good description of the geometry.

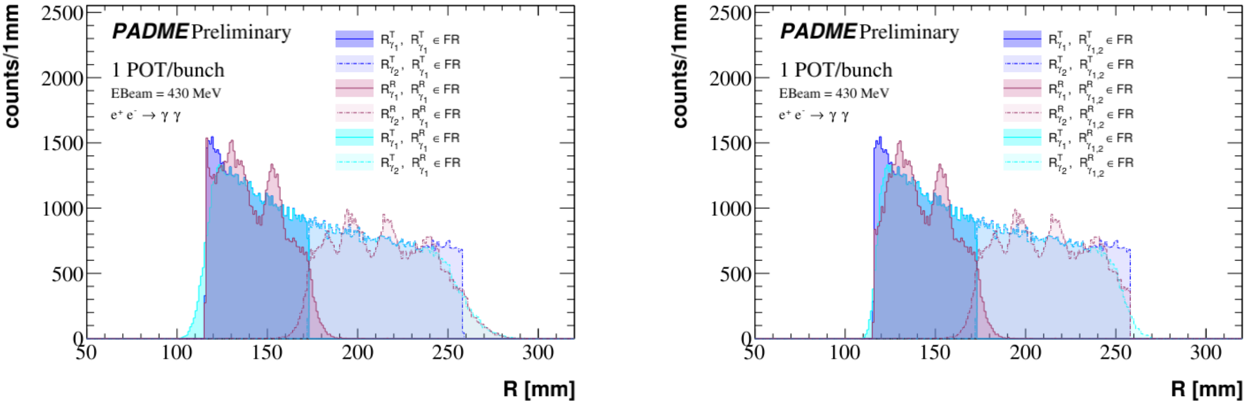

(a) (b)

Figure 1.11: *Distribution of true and reconstructed radius of photons from annihilation events. Continuous lines refer to the most energetic photon γ_1, dotted lines to the other photon γ_2. Events are selected either for the first photon (a) and both (b) belonging to the fiducial region at MC truth level or at reconstruction level.*

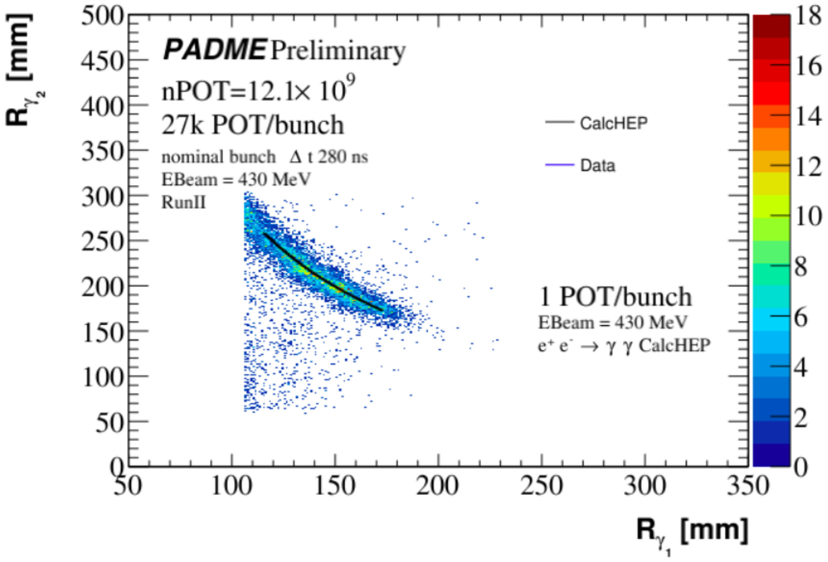

Figure 1.12: *Correlation between the radius of the first and second photon. Points are PADME data after a tight selection of annihilation events, corresponding to cuts a,b,c,d,e presented in Section 1.4. The black line is the same correlation according to MC truth in CalcHEP.*

1.5.1 The acceptance at leading order

The acceptance of the fiducial region defined for the measurement was extracted as a global factor telling what fraction of the annihilation events reach ECAL in the FR. The effect of event migration at the boundary of the FR, which instead is a function of polar angle of the photons, will be estimated later and treated as a correction to the efficiency.

The global acceptance is given by

$$acc = \frac{N_{\gamma\gamma}^{gen} \in FR}{N_{\gamma\gamma}^{gen}} \tag{1.10}$$

where $N_{\gamma\gamma}^{gen} \in FR$ if the number of the annihilation events generated by CalcHEP generation that fall in the FR, and $N_{\gamma\gamma}^{gen}$ is the total number of the generated events. The sample used for this study consist of 10^6 annihilation events, and the number of the annihilation events observed in the FR is $\sim 65,3 \times 10^3$, thus the global acceptance is $A = 0.0653 \pm 0.0003$ where the error comes from the statics of the MC sample.

1.5.2 A correction for migration effects

In the PADME data the cut used to decide if an event belongs to the FR are applied to values of R_γ that are reconstructed from quantities measured by the detector. The simulation of the CALCHEP sample can be used to understand how the number of events that are truly in the FR, $N_{\gamma\gamma}^{gen} \in FR$, relates to the number of events that are reconstructed, in the assumption of full efficiency, within the FR, $N_{\gamma\gamma}^{reco} \in FR$. The ratio,

$$A_{mig}(\theta_1, \theta_2) = \frac{N_{\gamma\gamma}^{reco} \in FR}{N_{\gamma\gamma}^{gen} \in FR} \tag{1.11}$$

will need to multiply the event dependent efficiency at the denominator of Equation 1.1.

In order to disentangle the efficiency effects from migration effects, the correction A_{mig} has been estimated using a smearing of the polar angle of the photons from the MC truth and comparing with distributions at generator level. The gaussian smearing was defined using the data, and looking at the width of the distribution of the reconstructed polar angle of a given photon, once the value of theta for the other is set to a constant value. This width of the distribution was found to have a negligible dependence on the polar angle and to be equal to $\sigma_\theta = 2.04$ mrad. After that, the following samples of events are in hands:

1. annihilation at generator le events from CalcHEP in the entire phase space;
2. annihilation at generator leevents from CalcHEP in the entire phase space with both photon polar angles smeared by σ_θ.

The correction is measured as:

$$A_{mig}(\theta) = \frac{N_{\gamma\gamma}^{smeared}(\theta_i)}{N_{\gamma\gamma}(\theta_i)} \tag{1.12}$$

where $N_{\gamma\gamma}^{smeared}(\theta_i)$ is the number of photons of the smeared sample with a polar angle equal to θ_i, and $N_{\gamma\gamma}(\theta_i)$ is the number of photons generated with a polar angle equal to θ_i.

The first step is to select all the events in the samples 1. and 2. that have $R_{\gamma_1} \in FR$ and study the distributions of the polar angle of both photons. These are shown in Figure 1.13 (a),

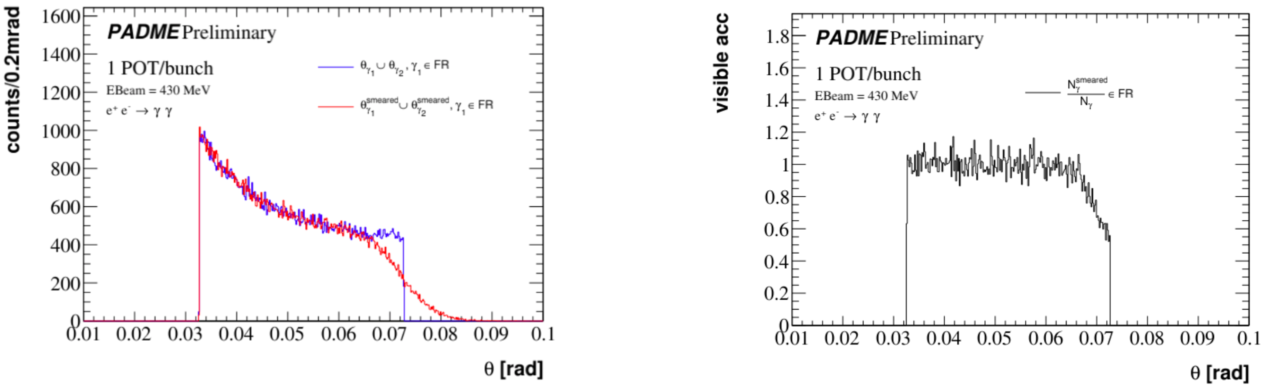

(a) **(b)**

Figure 1.13: *(a) Distribution of the polar angle of the two photons of the annihilation sample, in blue the CalcHEP generation, in red the same sample after the smearing in theta. The selection for this events is* $R_{\gamma_1} \in FR$. *(b) The visible acceptance calculated as the ratio between the number of annihilation in a single bin for the sample with the smearing over the sample from the generator (red line / blue line of the Figure (a)).*

in blue for MC truth and in red for the smeared sample. The ratio of the two distribution, as described in Equation 1.12, is represented in Figure 1.13 (b). This shows that if the event selection enforces the FR cut corresponding to the acceptance through a request applied only to one photon[3], in this case the most energetic one, the correction for migration effects it be applied as function of θ_{γ_1} is always compatible to one.

On the other hand if the event selection requires that both photons are reconstructed in the FR, the correction for migration effects, applied again per event as a function of θ_{γ_1} (or θ_{γ_2}), depends on the event topology, as shown in Figure 1.14. Here, the distributions of the polar angles for both photons are shown after selecting all the events in both smeared and MC truth samples with both photons in the FR. The ratio of the two distributions, as described in Equation 1.12, is shown in Figure 1.14 (b). In this case, the correction is not identically equal to one.

1.5.3 Acceptance at NLO

The CalcHEP generator produces annihilation events, with exactly two photons in the final state, at the leading order in the perturbative expansion. It can also be used to produce the process $e^+e^- \to \gamma\gamma(\gamma)$ at the leading order approximation; Eventually the two samples might be combined to derive a general estimate for the inclusive cross section for the process e^+e^- to photons, however this procedure is prone to theoretical inaccuracies. On the other hand, Babayaga is NLO event generator for the $e^+e^- \to \gamma\gamma$ process, which means that the

---

[3] One has to remember that in terms of acceptance, i.e. when considering generator level quantities, requiring only one photons in the FR is perfectly equivalent to requiring both photons in the FR.

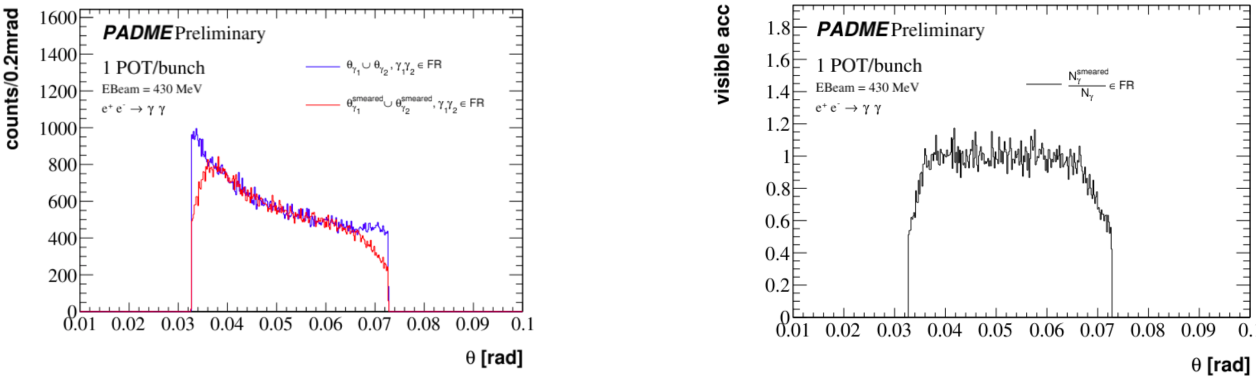

(a) **(b)**

Figure 1.14: *(a) Distribution of the polar angle of the two photons of the annihilation sample,for CalcHEP generation (blue) and after the smearing in polar angle (red). The selection for this events is both the photon* $R_{\gamma 1}, R_{\gamma 2} \in FR$*. (b) Visible acceptance calculated as the ratio between the number of annihilation in a single bin for the sample with the smearing over the truth sample (red line / blue line of the Figure (a).)*

production of two and three photons are consistently managed over the phase space. In addition, Babayaga can be configured to run in the LO approximation, therefore a first check done to verify the compatibility of the LO predictions from the two generators. The total cross sections obtained are $\sigma(e^+e^- \to \gamma\gamma)^{CalcHEP} = 1.91218$ mb and $\sigma(e^+e^- \to \gamma\gamma)^{Babayaga} = 1.91096 \pm 0.00036$ mb with a relative difference of 0.06%. Another check was done to compare the kinematics measuring the global acceptance of the process. In this case the one measured with Babayaga is $acc^{Babayaga} = 0.0651$, thus there is a relative difference of -0.4% with the acceptance measured with CalcHEP. After these preliminary check a sample of the process $e^+e^- \to \gamma\gamma(\gamma)$was generated. When running Babayaga at NLO up to three photons can be generated and the three photon final state is not anymore fully constrained. In this case the spatial resolution of ECAL should be considered if a soft photon falls close to another one, they may be reconstructed as a single cluster. To take into account this clustering effect photons from Babayaga are merged if the second lies at a distance in X or Y from the other compatible with the clusterization algorithm. In this case the resulting merged photon is assigned an energy equal to the sum of the two original energies and a position computed as an energy weighted average of the original positions. After this procedure, the photons are requested to pass the kinematic cuts that will be applied in the event selection: $E_\gamma > 90$ MeV and $|\Delta E| = |E_\gamma - E(\theta_g)| < 100$ MeV. Notice that these conditions in a LO simulation are trivially satisfied, therefore they ere not applied to estimate the Acceptance in the LO approximation. The events where at least one pair of photons passing the kinematic cuts and lying both inside the FR are counted as events inside the acceptance. The ratio of this number to the total number of events produced by Babayaga is used to assess the acceptance that is measured to be: $A = 0.06341 \pm 0,00026$ that is relative 2.6% lower than the acceptance at the leading order.

This is used to measure the cross section as described in the next sections.

The systematics that can affect the acceptance come from perturbative approximation and the error on the distance between the target and the ECAL detector. For the first of them the NNLO correction is quoted be of the order of 0.1% put reference, hence it can be neglected. For the second the variations of the acceptance when changing the distance between ECAL and target have been estimated and they are summarized in Table 1.4 . Since the systematic error the measurement of the distance from the survey of the PADME apparatus is $\sim few$ mm, also this systematic uncertainty can be neglected.

Table 1.4: *Acceptance calculation obtained varying the distance between ECAL and target.*

Variation [mm]	$acc^{Babayaga}$	$\frac{acc^{Babayaga}}{acc_0^{Babayaga}}$
-15	0.0627771	0.990
-10	0.0629869	0.993
-5	0.0632111	0.997
0	0.0634096	1.000
$+5$	0.0632002	0.997
$+10$	0.0629825	0.993
$+15$	0.0627801	0.990

1.6 Efficiency determination and closure tests

The photon efficiency was measured on data by developing a tag and probe technique exploiting the closed kinematics of annihilation events. Typically data driven efficiency measurements benefit from another auxiliary detector that allows to observe a sample of reference particles (probes), sometimes identified as belonging to a specific category of interest thanks to a tagging criterion. Then, the efficiency for reconstructing and identifying that category of particles with the detector and procedure under test is measured as the number of probes that are actually matched a particle reconstructed by the detector or procedure under test. For example, in a detector with a central spectrometer IS tracking all charged particles and an outer spectrometer OS for muons, the OS efficiency can be measured by looking for a well reconstructed muon reconstructed (tag) that combined with a track (probe) reconstructed in the IS gives an invariant mass corresponding to the J/Psi mass; the OS efficiency is given by the number of probes that have a matching muon track in the OS divided by the total number of probes.In the case of annihilation events in PADME calorimeter is a destructive detector and there is no other tagging detector to confirm the presence of a photon. Therefore the redundancy of kinematic constraints in the annihilation process is used to define a tag, a probe and to test if the probe is matched.

1.6.1 Tag and probe with annihilation events in PADME

As already extensively discussed, the two photons produced in the final state of $e^+e^- \to \gamma\gamma$ are correlated in energy and in space. Figure 1.15 shows that the polar angle of an annihilation photon predicts its energy, through an analytical function $E = f(\theta)$. Therefore, if a photon in ECAL comes from annihilation:

- its energy is compatible with $E_\gamma = f(\theta_\gamma)$;
- a second photon must exist back to back in phi to the first with $E_{\gamma 2} = E_{beam} - E_{\gamma 1}$;
- the energy of the second photon is also compatible with $E_{\gamma 2} = f(\theta_{\gamma 2})$.

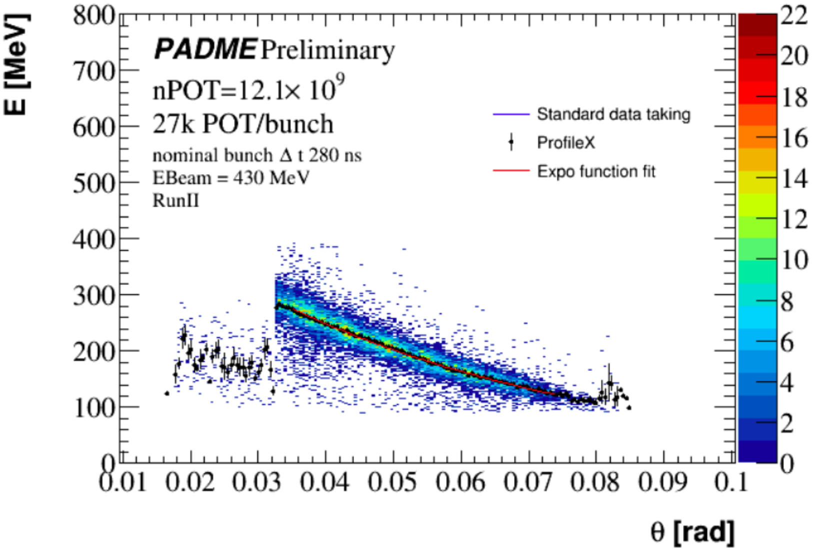

Figure 1.15: *Correlation between the energy E and the polar angle θ of annihilation photons. For the plot are used data of run II and events that pass the selection: a,b,c,d,e, described in Section 1.4, to be background free.To extract the function $f(\theta_g)$ used in this studies to extract the predicted energy of the photon, a profileX was done, thus an exponential fit on a good region of it (fitted in* $[0.035, 0.074]$ rad *to exclude the problematic points). The parameters extracted are used to convert the polar angle in energy.*

Therefore, the tag is identified as a cluster in the FR of ECal with:

$$\Delta E_{tag} = E_{Tag} - f(\theta_{Tag}) \tag{1.13}$$

close to zero. All the clusters in the FR with $|\Delta E_{Tag}| < 100$ MeV are considered tag candidates. This is a very loose cut considering that the resolution on ΔE_{Tag} is of the order of ~ 15 MeV.

When a tag candidate is found, the probe is defined as the “expected second photon” from the annihilation therefore, the number of probes is equal to the number of tags.

Finally, a matched probe candidate is defined as a cluster with features similar to the probe hypothesis; this means with $|\phi - \phi_{Probe}| < 25$ Deg, with $|\Delta E_{Probe}| < 100$ MeV, where $\Delta E_{Probe} = E_{Probe} - f(\theta_{Probe})$, and with $|\Delta E_{TP}| < 100$ MeV, where $\Delta E_{TP} = E - E_{beam} + f(\theta_{Tag})$. In addition, a matched prove is requested to be in time with the tag photon within 7 ns.

If more than one cluster seems to match a given tag, a choice must be taken; this is done by selecting the candidate matched probe with the minimum χ^2 defined as follows:

$$\chi^2 = \frac{\Delta E'^2 + \Delta E^2_{probe}}{\sigma^2} = \frac{\Delta E^2_{Probe} + \Delta E^2_{TP}}{\sigma(E_{\gamma_1})^2 + \sigma(E_{\gamma_2})^2} \tag{1.14}$$

where $\sigma(E_{\gamma_i})$ for $i = 1, 2$ is the energy resolution of the calorimeter and it is considered equal to 15 MeV for all the clusters. An additional analysis was made requesting the belonging of the second photon in the FR. In the following studies, in order to understand each element of the analysis, the efficiency and the corrected annihilation yields are reported for both the selections: γ_1 in FR and γ_1, γ_2 in FR.

Finally, given the sample of tag candidates, the counting of the "signal candidates" N^{sig}_{Tag}, i.e. of the photons that are really originating from an annihilation, requires the subtraction of a large background; similarly, the counting of the matched probes, N^{sig}_{Probe}, in the sample of candidates requires the subtraction of a background that, in this case, is very small.

The efficiency is therefore computed as follows:

$$\epsilon \pm \sigma = \frac{N^{sig}_{probe}}{N^{sig}_{tag}} \pm \sqrt{\frac{N^{sig}_{probe}}{(N^{sig}_{tag})^2} + \left(\frac{N^{sig}_{probe}}{(N^{sig}_{tag})^2}\right)^2 \times N^{sig}_{tag}} \tag{1.15}$$

The error takes into account the poisssonian fluctuation of both counters because the background, dominating the selection of tag candidates, washes out the correlation of numerator and denominator that would require a binomial treatment.

Indeed the subtraction of the background contaminating the sample of candidate tags and the determination of the number of signal tags is the most critical step in the procedure and several approaches have been adopted. The first strategy consists in modelling the background using the sideband or a control data sample, applying a gaussian fit to the signal peak to estimate its standard deviation; The number of tags is then computed as the integral of the background subtracted distribution in the range corresponding to 3 sigma. The same procedure is applied to count the number of matched probes in the sample of candidates. An assessment of the systematic error affecting the efficiency determination is obtained by estimating the number of tags and probes consistently as the integral within 1 or 5 sigma of the background subtracted candidate distribution.

This method has been applied to measure the efficiency in 16 bins covering the ECAL geometry, two radial bins and 8 azimuthal bins.

1.6.2 Validation in MC

The entire methodology was tested on MC samples of different types: pure annihilation events in a perfect PADME detector, annihilation events overlapped to a realistic pileup of other interactions, with and without defects in the calorimeter.

Efficiency from MC truth

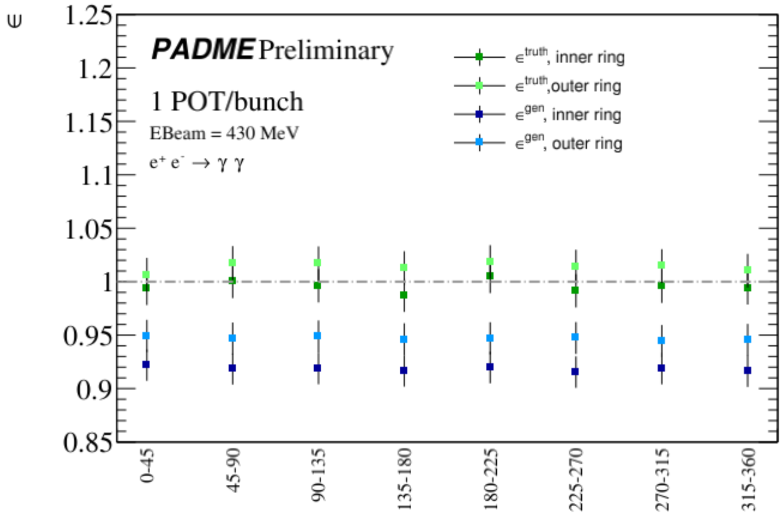

Figure 1.16: *True and effective efficiency for photons from annihilation events, in the absence of pileup and detector defects. The efficiency is quoted in 8 bins in phi each divided in 2 bins in R.*

A preliminary study tried to address the relation between true photons and reconstructed photons in a perfect ECAL, without detector defects nor pileup. ECAL was divided in 8 azimuthal slices and each one in two radial intervals: $R_{min} - R_{mid}$ and $R_{mid} - R_{max}$. In each event the photon spatial coordinates from the MC truth and from the reconstruction of the same events simulated with PADMEMC are studied. The following quantities are studied

- effective efficiency, defined as the ratio between the number of reconstructed photons and the number of generated photons in each bin $\epsilon^{truth} = \frac{N_\gamma^{sim}}{N_\gamma^{gen}}$. This is shown in Figure 1.16 for each bin (green dots), where N_γ^{sim} is the number of annihilations observed in that bin analysing the simulated sample and N_γ^{gen} is the number of annihilation recorded in the same bin studying the truth information. A first observation is that in some bins the effective efficiency is higher than 1 due to a migration effect. Indeed, the photon reconstructed coordinates are modified by the resolution and segmentation of the detector and by the presence in the experiment of all the components. This effect is observed in all bins of the outer ring;

- true efficiency, given by the ratio between the number of the simulated photons having true and reconstructed spatial coordinates in a bin and the number of the generated γ that fall in the same bin $\epsilon^{gen} = \frac{N_\gamma^{sim}(\gamma^{gen})}{N_\gamma^{gen}}$, where $N_\gamma^{sim}(\gamma^{gen})$ is the number of the annihilations having truth and simulated coordinates in the bin. This is shown by the light blue points in figure 1.16. The truth efficiency in the outer ring $[R_{mid} - R_{max}]$ is systematically higher then the inner ring $[R_{min} - R_{mid}]$ due to a stronger loss (migration toward the outside) for resolution in the inner region.

Tables 1.5 (for the inner ECAL ring) and 1.6 (for the outer ECAL ring) report for all the azimuthal slices the truth efficiency ϵ^{truth}, the efficiency ϵ, the feed-through and loss at the inner and at the outer boundary are summarised. The feed-through at the inner boundary is defined as the ratio of the number of clusters simulated in that bin but with the truth at $R_\gamma < R_{min}^{range}$ to the total number of clusters in the bin. The loss at the inner boundary is the ratio between the number of clusters simulated with a radius $R_{cl} < R_{min}^{range}$ but with the truth with radius in the bin. Analogous definitions are used for the feed-through and loss at the outer boundary.

Table 1.5: *True and effective efficiency, feed-through and loss at the inner and outer boundary of the bin for photons from annihilation events, in the absence of pileup and detector defects. The efficiency is quoted in 8 phi bins for R in* $[R_{min}, R_{mid}]$.

Angle range	ϵ **truth** ± 0.015	ϵ ± 0.016	feed through in ± 0.002	loss in ± 0.002	feed through out ± 0.002	loss out ± 0.002
$[0, 45[$	0,923	0,994	0,046	0,044	0,030	0,034
$[45, 90[$	0,918	1,000	0,050	0,046	0,029	0,037
$[90, 135[$	0,919	0,996	0,047	0,045	0,028	0,037
$[135, 180[$	0,917	0,987	0,047	0,050	0,031	0,033
$[180, 225[$	0,920	1,005	0,047	0,044	0,029	0,036
$[225, 270[$	0,915	0,994	0,049	0,048	0,028	0,036
$[270, 315[$	0,919	0,996	0,048	0,050	0,034	0,033
$[315, 360[$	0,916	0,994	0,046	0,049	0,029	0,035

Tag and probe on MC

A first study was done in simulated single annihilation events, ignoring pileup and defects of the detector. For this reason the selection of the tag and of the matched probe are free from any background. In this case the number of tags (matched probes) in measured by integrating 3σ the peak of the distribution of ΔE_{tag} (ΔE_{probe}). The systematic errors are estimated as described in section 1.6.1. Figure 1.17 shows in blue the tag-and-probe efficiency defined as the number of matched-probes divided by the number of tags; in red the tag-and-probe efficiency within the fiducial region is defined as the number of matched probes in the fiducial region divided by the number of tags. Error bars represent the statistical error σ while the shaded band corresponds to the total error $\sigma \oplus \sigma_{sys}$ including the systematic uncertainty.

Table 1.6: *True and effective efficiency, feed-through and loss at the inner and outer boundary of the bin for photons from annihilation events, in the absence of pileup and detector defects. The efficiency is quoted in 8 phi bins for R in* $[R_{mid}, R_{max}]$.

Angle range	ϵ truth ±0.015	ϵ ±0.016	feed through in ±0.002	loss in ±0.002	feed through out ±0.002	loss out ±0.002
$[0, 45[$	0,949	1,020	0,035	0,030	0,027	0,021
$[45, 90[$	0,947	1,017	0,040	0,027	0,030	0,026
$[90, 135[$	0,949	1,017	0,039	0,026	0,033	0,026
$[135, 180[$	0,946	1,013	0,034	0,030	0,027	0,024
$[180, 225[$	0,947	1,018	0,036	0,029	0,027	0,024
$[225, 270[$	0,947	1,014	0,037	0,024	0,033	0,028
$[270, 315[$	0,945	1,015	0,035	0,031	0,032	0,024
$[315, 360[$	0,946	1,010	0,035	0,028	0,027	0,026

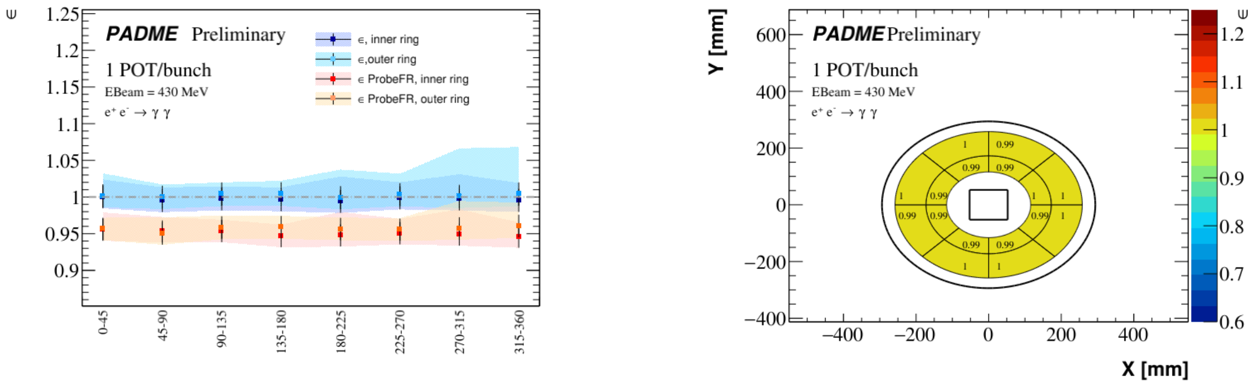

(a)

(b)

Figure 1.17: *Tag and probe efficiency estimated for photons from annihilation events, in the absence of pileup and detector defects. The efficiency is quoted in 8 bins in phi each divided in 2 bins in R. (a) The efficiency is quoted with (red) and without (blue) the requirement that the matched probe belongs to the fiducial region. (b) Schematic view of the efficiency without any requirement.*

Comparing truth and tag and probe efficiency

The definitions based on MC truth and shown efficiency in Figure 1.16 differ from those based on the tag and probe technique represented in Figure 1.17. However, a comparison between $\epsilon^{truth} = \frac{NClusters_i}{NTruth_i}$ of the Figure 1.16 (green dots) and the tag and probe efficiency without the request for the matched probe to be in the FR $\epsilon^{TP} = \frac{nProbe_i}{nTag \in bin_j}$[4] can be done. As discussed in Section 1.6.2, the differences between the efficiency in the inner bins and in the outer ring Figure

---

[4] In this nomenclature the subscript i means the bin in which ECAL efficiency is studied, while j is the bin with opposite azimuthal angle and opposite radius range (constrain given by the kinematics of the annihilation).

1.16 is due to migration effects. In the tag and probe efficiency trend this effect is reduced. In addition the efficiency is never higher than 1 because the existence of a probe is constrained to the existence of a tag, so also when the number of tags is lower than the number of clusters in the opposite bin (case of tag in bins of the inner ring as described in 1.6.2), the number of probes can't be higher than the number of tags. When the number of tags is higher than the number of clusters in the opposite bin (case of the tag in the outer ring) the absence of an explicit boundary between inner and outer ring for the probe allows to find a matched probe, so the efficiency is still close to one. From these considerations it follows that the efficiency extracted from tag and probe is more stable when moving from an inner to an outer bin. The small differences in the tag and probe efficiency are induced by cluster reconstruction.

Table 1.7 summarized the ratio between the effective efficiency from MC truth and the one measured with the tag and probe (TP):

$$\alpha = \frac{\epsilon^{truth}}{\epsilon^{TP}} = \frac{\frac{NClusters}{NTruth}}{\frac{NProbe}{NTag}}. \tag{1.16}$$

for all the phi slices, inner and outer rings. In the inner ring bins the truth and TP efficiencies are equal within the 1%, while in the outer ring the truth efficiency is higher than the TP one because more affected by migration effects.

Table 1.7: *Ratio between the effective truth derived from MC and TP efficiency.*

Angle range	α inner ring	α outer ring
$[0, 45[$	$0,994$	$1,018$
$[45, 90[$	$1,004$	$1,018$
$[90, 135[$	$0,999$	$1,013$
$[135, 180[$	$0,991$	$1,009$
$[180, 225[$	$1,011$	$1,019$
$[225, 270[$	$0,995$	$1,011$
$[270, 315[$	$0,999$	$1,014$
$[315, 360[$	$0,999$	$1,006$

1.7 Closure tests on simulation

1.7.1 Tag and probe efficiency and detector defects

To test how the tag and probe efficiency depends on detector defects, the CalcHEP sample $e^+e^- \to \gamma\gamma$ was simulated emulating four dead crystals in ECAL in the bin $\phi \in [45, 90]^\circ$ in order to induce an important localised defect. Figure 1.18 shows the map of the annihilation photons for this special sample.

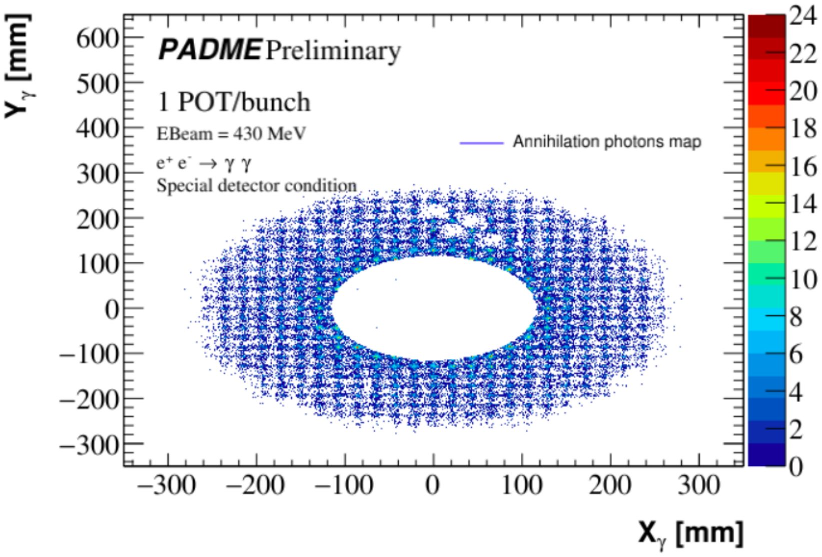

Figure 1.18: *Map of the annihilation photons selected with only the time coincidence requirement and the application of the FR to the most energetic photon. This is a special simulation with four dead crystals, made to test the tag and probe efficiency.*

First the effective efficiency for this special sample was estimated using the knowledge of MC truth as described in section 1.6.2. The dependence on the bin in ECAL is shown in Figure 1.21 (a). As expected the efficiency is lower in the region where the detector response is affected by the dead crystals. Then the ΔE_{Tag} and ΔE_{Probe} were studied to extract the tag and probe efficiency. The distribution of these variables in this special sample are not gaussian for all the bins. Figure 1.19 shows the distribution of ΔE_{tag} for tags reconstructed in a bin

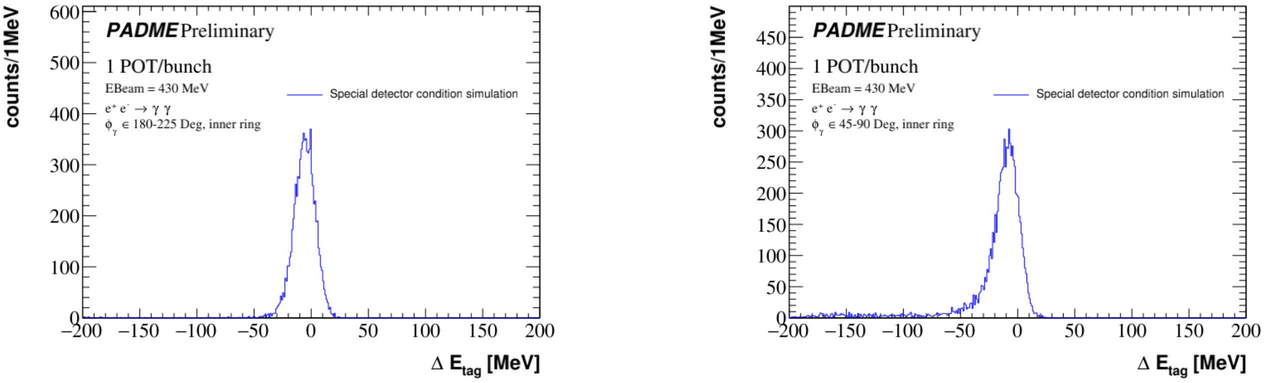

(a) (b)

Figure 1.19: ΔE_{Tag} *distribution for the MC simulation of pure annihilation events in a simulation where the detector has dead channels. On the left the distribution is plotted for a bin without dead crystals, on the right the same distribution for tags reconstructed in the bin with dead crystals.*

without problems $\phi \in [180, 225]$ Deg , R $\in]\mathrm{R}_{\mathrm{min}}$ and $\mathrm{R}_{\mathrm{mid}}[$ while Figure 1.19 (b) the same distribution observed for the problematic bin with $\phi \in [45, 90]$ deg and R $\in]\mathrm{R}_{\mathrm{min}}, \mathrm{R}_{\mathrm{mid}}[$. The probe distributions are affected by the same problem as indicated by Figure 1.20 where the ΔE_{Probe} distributions are reported for the same bins. Also for this variable is visible a tail appears where there are dead crystals. The procedure applied to measure the tag and probe efficiency is the one described in the previous section and the efficiency obtained is reported in Figure 1.21 (b). In the ECAL slice where four dead crystals were simulated the efficiency is strongly reduced $\epsilon \sim 0.86$. The corresponding increase of the efficiency in the opposite phi slice shows that the efficiency extracted using the tag and probe is biased. This is due to the counting procedure for tags and probes (applied in a 3σ interval around the peak) that looses a fraction of tags or probes if the distributions exhibit a long tail due to inaccurate energy and position measurement induced by the detection holes.

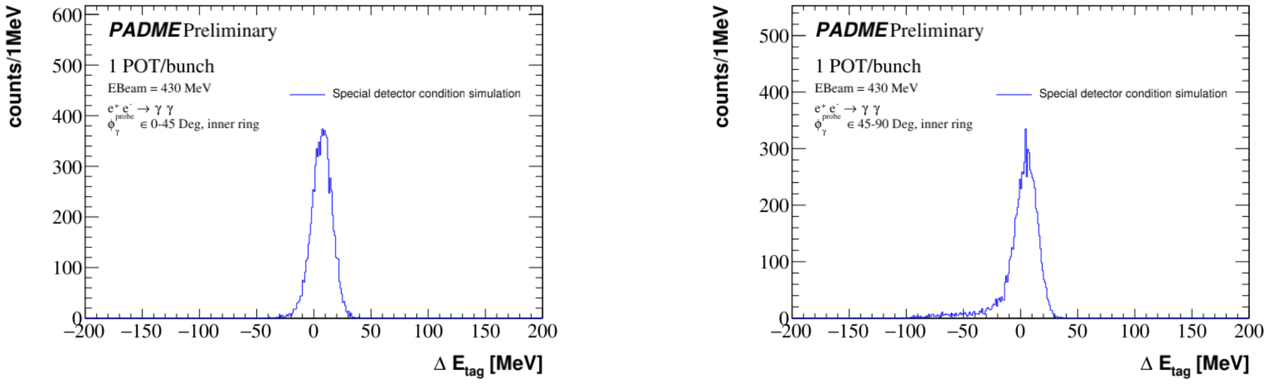

(a) **(b)**

Figure 1.20: ΔE_{Probe} *distribution for the MC simulation of pure annihilation events in a simulation where the detector has dead channels. On the left the distribution is plotted for a bin without dead crystals, on the right the same distribution for tags reconstructed in the bin with dead crystals.*

These biases make difficult to give an interpretation to the tag-and-probe efficiency. However, it turns out to be still a useful quantity. Since the correction of the annihilation yield will be done using $\epsilon(\gamma_1) \times \epsilon(\gamma_2)$ the opposite biases compensate each other. Indeed in the problematic region the efficiency is $0,86 \times 1,08 = 0,93 < 1$. Figure 1.22 (a) shows the truth (green) and TP (blue) event efficiency. The event efficiency from the tag and probe in the problematic bins is slightly lower than the truth event efficiency. This is an expected effect because in the truth efficiency there is no use of the cluster energy. A photon hitting a dead crystal likely produces a small signal in a nearby crystal. The tag and probe selection rejects this cluster (because its energy is not compatible with the expected value). On the other hand, the simple counting of clusters used for the truth efficiency is still taking into account that photon. If an energy threshold is applied when counting clusters to estimate the truth efficiency, the two efficiency determinations become statistically the same, as shown in Figure 1.22 (b).

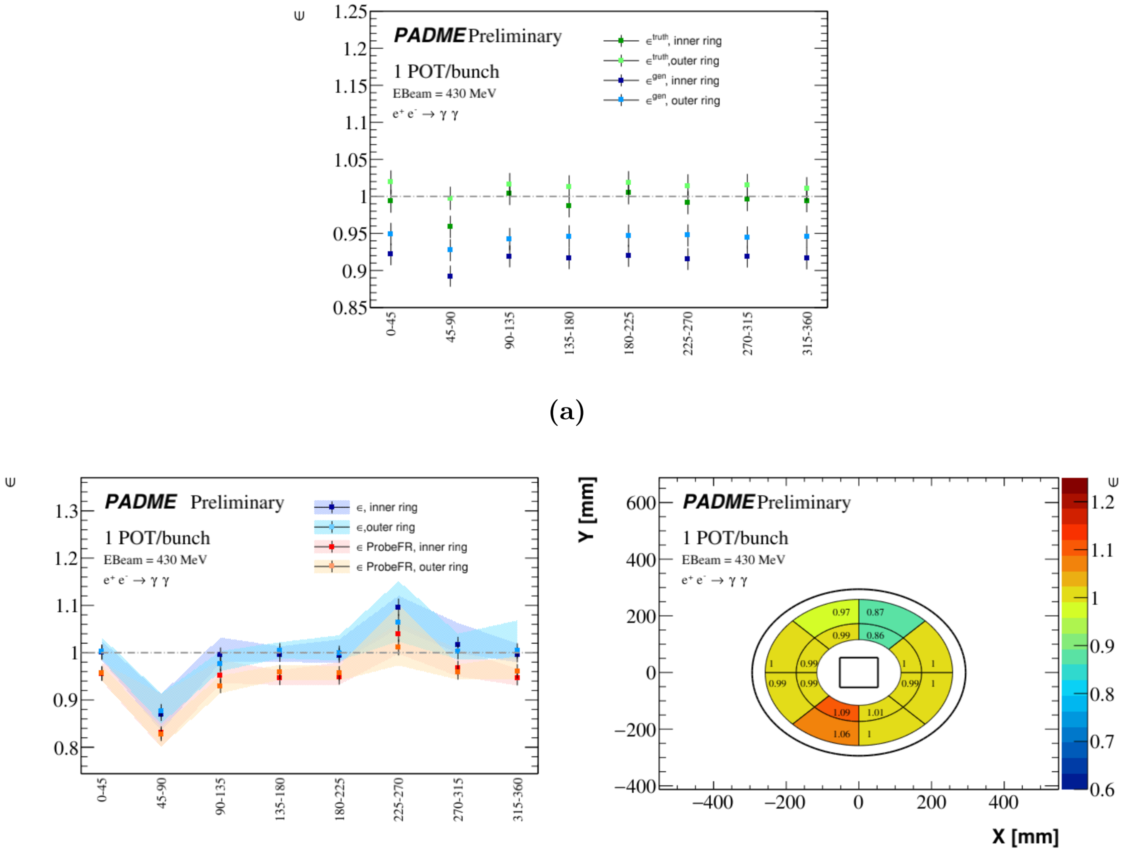

(a)

(b) (c)

Figure 1.21: *Efficiencies on a simulation where the detector has dead channels. (a) Truth efficiency based on Monte Carlo. (b) Efficiency based on the tag and probe technique. (c) Schematic view of the TP efficiency without any requirement*

1.7.2 Measurement strategy based on tag and probe efficiency

The simulation of single annihilation events generated by CALCHEP detector defects and no pileup is used to verify the consistency with truth of the yield of annihilation events after correction for migration at the acceptance boundary and reconstruction efficiency as measured as in data. The simulation described four dead crystals. The tag and probe single photon efficiency for this sample is shown in Figure 1.21. The annihilation candidates are assigned weights described in Figure 1.22.

When candidates are selected requiring the the most energetic photon is in the fiducial region, the efficiencies to be assigned to the photons are the tag and probe efficiency obtained without requiring that the matched probe belongs to the FR and the correction for the migration at the acceptance border in given by Figure 1.13. On the other hand, when the selection requires that both photons are in the FR, the efficiency to be used for the second photon is the one obtained by requiring that the matching probe belongs to the FR and the correction for the

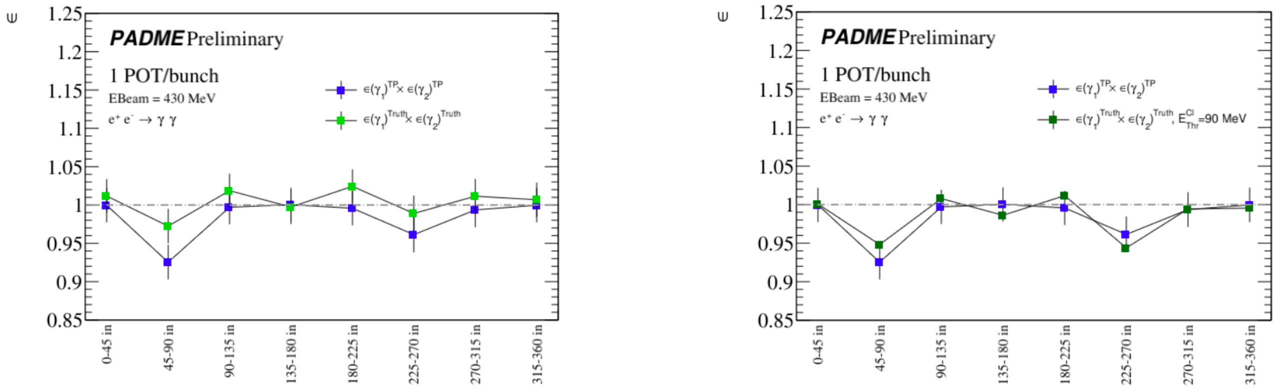

(a) **(b)**

Figure 1.22: *Event efficiency given by* $\epsilon(\gamma_1) \times \epsilon(\gamma_2)$*. On the right, the clusters used for the truth efficiency have a reconstructed energy above* 90 MeV*.*

migration at the border of the acceptance is in Figure 1.14. This is equivalent to using the efficiency measured with matched probes within the FR for both photons and the correction for migration at the acceptance border in Figure 1.13.

The yield of the annihilation candidates, for this background free sample, is given by the integration of the $ECAL_{g_1} + E_{\gamma_2}$ spectrum in the energy range $[300, 600]$ MeV. Figure 1.23 shows the annihilation peak of all the events that pass the time selection, with the first photon in the FR and the CoG coordinates in 5 cm. Original and corrected yields extracted are reported in Table 1.8. After applying the correction for efficiency and migration at the acceptance boundary the reconstructed yield matches within an error of 0.5% the number of events in the acceptance known from MC truth. This successful closure test validates the tag and probe efficiency measurement and the cross section measurement strategy also in case of local defects of the detector.

Table 1.8: *Annihilation candidates reconstructed in a simulation with detector defects and no pileup. The number of candidates after correction for efficiency and acceptance corrections is also reported along with the number of events in the acceptance at generator level.*

Sample and cut	$\gamma_1 \in FR$	$\gamma_1, \gamma_2 \in FR$
CalcHEP **generation** (expectation)		
$\in FR$	65320	65318
CalcHEP **simulation**		
$\in FR$, $\lvert CoG\rvert < 5$ cm	64006	61041
$\in FR$, $\lvert CoG\rvert < 5$ cm, corrected for $\epsilon_{TP} \times \epsilon_{TP}(\times \epsilon_{TP,probe \in FR})$	65057	65088
$\in FR$, $\lvert CoG\rvert < 5$ cm, corrected for $\epsilon_{TP} \times \epsilon_{TP} \times Acc(\theta_{\gamma_1})$		65649

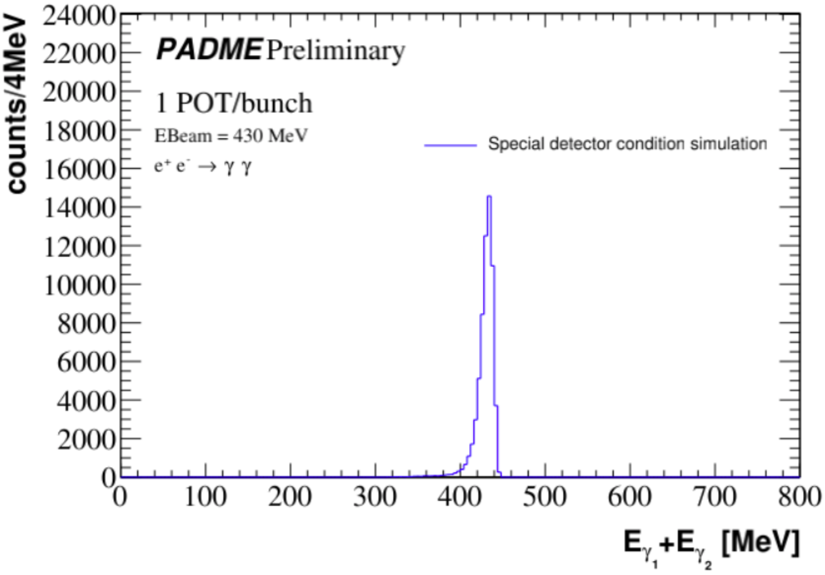

Figure 1.23: *Distribution of the sum of the two photons energy* $E_{\gamma_1} + E_{\gamma_2}$ *for all the events that pass the time selection, with the first photon in the FR and that has the CoG coordinates inside* 5 cm *for a MC sample of single annihilation events and four dead crystals in ECAL .*

1.7.3 Measurement strategy based on scale factors

Another strategy for the cross section measurement is to use the efficiency predicted by simulation and corrected with scale factors that allow to match the efficiency in data. The method has been introduced in Section 1.1 and is referred as the “scale factor method”. Here, it will be applied in a special simulation. The tag and probe efficiencies will be used to compute scale factors in a sample of events playing the role of data (with defects) and in a sample of events playing the role of simulation.

Emulating a data and a MC sample

The simulation of annihilation events from CalcHEP in a PADME Monte Carlo with four dead crystals in the top-right quadrant of ECAL (see a hit map in Figure 1.18) has been split in two sub-samples defined as “data” and “MC”:

- sub-sample 1, shown in green in Figure 1.24, is free from detector defects and plays the role of simulation. Sub-sample 1, the “MC” region, can be considered as an imperfect simulation of sub-sample 2, the “data” region. In particular, a one-to-one relation between “MC” and “data” regions is defined by a rotation of $\pi/2$, i.e., a photon at ϕ_L in the “MC” region simulates a photon at $\phi_L + \pi/2$ in the “data” region.

- sub-sample 2, shown in yellow in Figure 1.24, plays the role of data; the detector defects are all located in this region;

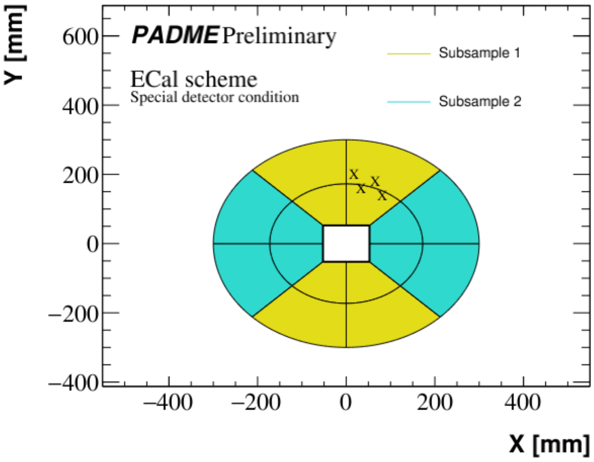

Figure 1.24: *Graphic representation of the two sub-samples.*

The number of annihilation events in the two samples, known from Monte Carlo truth and statistically compatible with each other, is reported in Table 1.9. Two simulations are studies: the first one with a single positron beam, the second with 25000 positrons in each event spread in 250 ns.

Table 1.9: *Number of annihilation events in the sub-sample 1 (MC role) and 2 (data role), known from Monte Carlo truth.*

Sub-sample	Yield
Data	32649
MC	32671

A pileup free simulation

In the absence of pileup, the number of annihilation candidates reconstructed in the “data” and “MC” regions are listed in Table 1.10, along with the selection criteria applied. As expected

Table 1.10: *Number of annihilation candidates reconstructed in the “data” and “MC” region from the integration of the distribution of* $E_{\gamma_1} + E_{\gamma_2}$ *in the range* $[300, 600]$ MeV*. Two selections are considered: the first requiring that the leading photon belongs to the FR, the second requiring that both photons are in the FR. No pileup is simulated.*

Sample	**Cut**	$\gamma_1 \in FR$	$\gamma_1, \gamma_2 \in FR$
Data	$\lvert\Delta t\rvert < 10$ ns, $\lvert X(Y)_{CoG}\rvert < 5$ cm	31443	29940
MC	$\lvert\Delta t\rvert < 10$ ns, $\lvert X(Y)_{CoG}\rvert < 5$ cm	32537	31088

the dead crystals are responsible of a lower yield in the "data" region.

As a first step each event passing the selection ($|\Delta t| < 10$ ns, $|X(Y)_{CoG}| < 5$ cm with the first or both photons in the FR) is reweighed according to Equation 1.3 using the tag and probe efficiency measured in the 16 bins and shown in Figure 1.21 (b). The corrected yields, reported in Table 1.11, are in agreement with the expected valued within 1%. It is interesting to observe that in the data region, where there are the dead crystals, the corrected yield is in agreement with the expectation, a confirmation that the bias of the efficiency, clearly visible in Figure 1.21 (b), is compensated in the product $\epsilon(\gamma_1) \times \epsilon(\gamma_2)$.

Table 1.11: *Yield extracted from the annihilation distribution obtained analysing the special detector calchep simulation and corrected for the weights as described in formula 1.3. The yields were extracted integrating the $E_{\gamma_1} + E_{\gamma_2}$ spectrum in a fixed range ($[300, 600]$ MeV).*

Sample	**Cut**	$\gamma_1 \in FR$	$\frac{\gamma_1 \in FR}{expetation}$	$\gamma_1, \gamma_2 \in FR$	$\frac{\gamma_1, \gamma_2 \in FR}{expetation}$
Data	$|\Delta t| < 10$ ns, $|CoG| < 5$ cm	32429	0.993	32477	0.995
MC	$|\Delta t| < 10$ ns, $|CoG| < 5$ cm	32598	0.998	32594	0.998

As a second step, the number of annihilation candidates is derived with the scale factor method.Therefore, each event in the MC region is rescaled with the product of two scale factors for the efficiency corresponding to each photons.

An efficiency scale factor is defined as follows:

$$f_i = \frac{\epsilon^{TP}(data|\phi_i, R_i)}{\epsilon^{TP}(MC|\phi_i, R_i)} = \frac{\epsilon^{TP}(data|\phi_i + \pi/2, R_i)}{\epsilon^{TP}(MC|\phi_i, R_i)} \tag{1.17}$$

where the efficiency at the numerator, estimated in the "data" region, is the efficiency measured at $\phi + \pi/2$. From these inputs and from the number of reconstructed candidates, the factor C, defined in Section 1.1 is computed and the efficiency-corrected yields summarized in Table ...... are obtained.

This was done for the two analyses related to the request of the most energetic photon or both in the fiducial region. All relevant counters are summarized in Table 1.12. The number of candidates reconstructed in the "data" region, after correction for the efficiency.

Applying this method it is obtained an yield close to the expected within $0,5\%$.

A simulation with pileup

The simulation used here is the sample of annihilation events from CalcHEP embedded on the GEANT4 simulation of the interaction of 25000 positrons with the target in each event corresponding to a beam bunch. This sample may contain annihilation processes simulated by GEANT4 and, therefore, not recorded in MC truth, in addition to the annihilation event generate by CalcHEP and embedded in the PADME simulation. To keep the ability of comparing reconstructed annihilation events with MC truth, reconstructed candidates are considered

Table 1.12: *Annihilation yield and scale factor from "MC" sample and yield after the selection and the correction for "DATA" sample.*

	DATA region		MC region	
	$\gamma_1 \in FR$	$\gamma_1, \gamma_2 \in FR$	$\gamma_1 \in FR$	$\gamma_1, \gamma_2 \in FR$
MC truth	32649		32671	
MC candidates			?	?
MC reweighed scale factor			31627	30065
C			0.968	0.920
Data candidates	31443	29940		
Data corrected for scale factor	32480	32535		

only if the two-photon kinematics matches the CalcHEP MC truth for that event. The performance of the matching logic is studied in a pure annihilation simulation without any dead crystals. The variables under study were the photon energy and azimuthal angle. The differences $\Delta E = E_\gamma - E_{cl}$ and $\Delta\phi = \phi_\gamma - \phi_{cl}$ between generated and reconstructed values for all events passing the selection cuts a, b and c described in Section 1.4 are shown in Figure 1.25 (a) and (b) for a pileup free simulation.

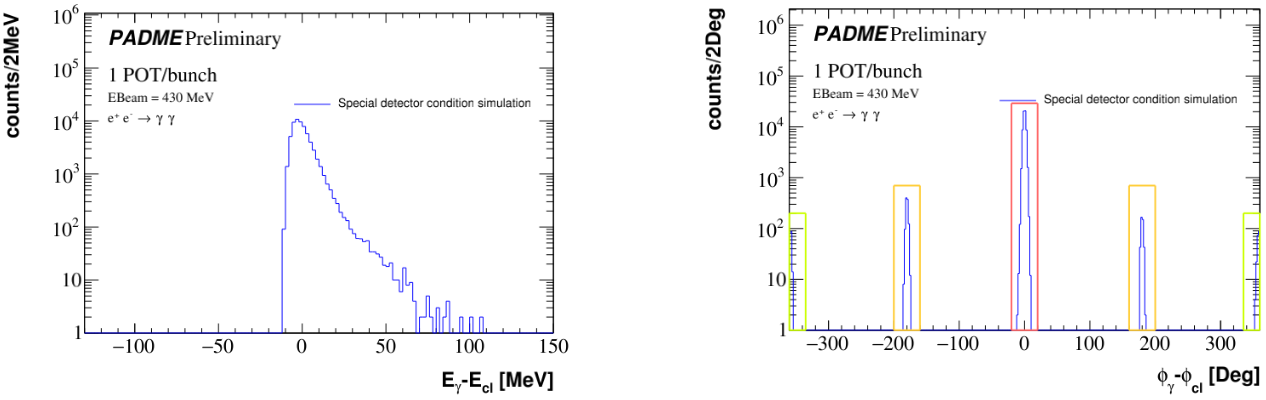

(a) (b)

Figure 1.25: *Left: distribution of $\Delta E = E_\gamma - E_{cl}$ for the events that pass the selection cuts a, b and c described in 1.4 for a pure annihilation simulation.*

The matching requirements applied are $|\Delta E| < 50$ MeV and $|\Delta\phi| = 180$ Deg(care is taken to treat correctly the case of $\Delta\phi = 180$ Deg , occurring when reconstructed photons are matched to the MC truth of the second photon in the event).

The effect of the matching is heavier when the detector has defects; this has been verified using the simulation of ECAL with 4 dead crystals in the top right quarter. The same procedures applied to this simulation separately for the data region (where defects lie) and the MC region (where the detector has no defects) gives counts summarised in Table 1.13. From these results, and from Table 1.10 where the number of annihilation events from MC truth is reported, the efficiency of the matching criterion in the data region is found to be $\beta = \frac{30809}{31443} = \frac{29313}{29940} = 0.98$ for the data region.

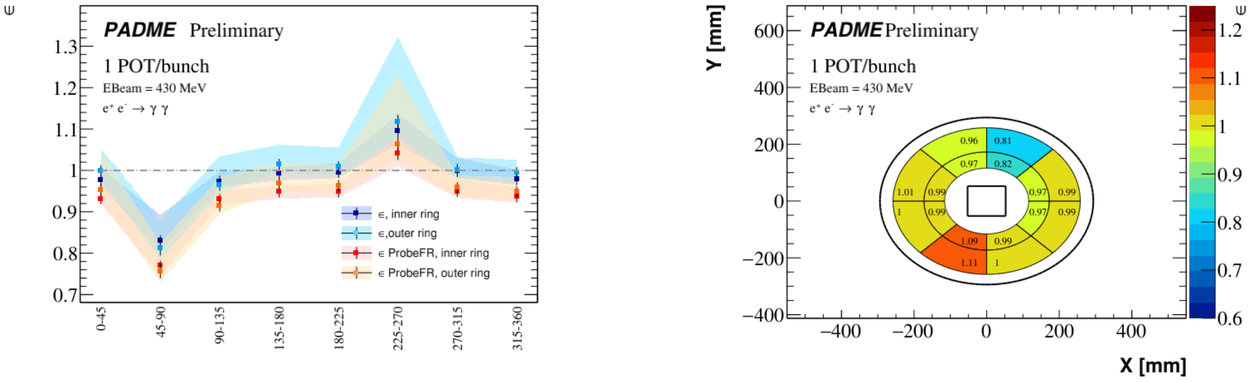

(a) (b)

Figure 1.26: *Tag and probe efficiency for MC simulation of CalcHEP with pileup. In (b) a schematic view of efficiency measured without any requirement.*

Taking these effects into account, the number of annihilation candidates selected in the sample with pileup is corrected with the tag and probe efficiency measured in the same sample shows in Figure 1.26. The results, reported in Table 1.14 for the data and the MC region, show a very good match with MC truth, both for the selection with the leading photon in the FR and for the selection with both photons in the FR.

After applying these requirements, the number of annihilation processes from CalcHEP passing the matching criterion was 65067 instead of 65172, corresponding to a 0.2% inefficiency of the matching criterion in absence of pileup and without any detector problems. In presence of pileup (25×10^3 POT/bunch) the number of annihilation that pass the MC truth matching is 65342, 0.3% more than expected (65172) due to a residual GEANT4 contamination.

Table 1.13: *Yield extracted from the annihilation distribution obtained analysing the special detector calchep simulation in order to extract the performance on the consistency selection.*

	$\gamma_1 \in FR$		$\gamma_1, \gamma_2 \in FR$	
Sample	Without consistency	Consistency applied	Without consistency	Consistency applied
Data	31443	30809	29940	29313
MC	32537	32489	31088	31042

In addition the scale factor method has been applied, following the same approach described for the simulation without pileup. The results are summarized in Table 1.15.

Table 1.14: *Yield extracted from the annihilation distribution obtained analysing the special detector calchep simulation with and without the consistency check corrected for the tag and probe efficiency.*

	$\gamma_1 \in FR$		$\gamma_1, \gamma_2 \in FR$	
Sample	Weighted w/o consistency	Weighted, Consistency applied	Weighted w/o consistency	Weighted, Consistency applied
Data	32429	31765	32477	32553
MC	32598	31784	32594	32548

Table 1.15: *Annihilation yield and scale factor from "MC" sample and yield after the selection and the correction for "DATA" sample applied to CalcHEP simulation with pileup.*

	DATA region		MC region	
	$\gamma_1 \in FR$	$\gamma_1, \gamma_2 \in FR$	$\gamma_1 \in FR$	$\gamma_1, \gamma_2 \in FR$
MC truth	32649		32671	
MC candidates			?	?
MC reweighed scale factor			31583	30022
C			0.967	0.919
Data candidates	31443	29940		
Data corrected for scale factor	32516	32579		

The results of the various closure tests performed in the simulation are very satisfactory also in the difficult case of pileup of interaction in a detector with some dead crystals.

In summary, a long list of checks discussed in this section allow to gain strong confidence on the tag and probe technique for the efficiency measurement and and the cross section measurement strategy that will be applied for the analysis of the PADME data.

1.8 Early selection studies

The analysis was run using the longest and stablest runs took during the second PADME run. For all the runs the energy of the beam is $E_{beam} = 430$ MeV, the pulse duration is $\Delta t \sim 280$ ns and the mean of the beam multiplicity is $N_{POT}/bunch \sim 27 \times 10^3$. The special runs took with the beam out of the beam line allow the prediction of the beam related background. These runs were used to subtract the background from tag, probe, and annihilation distributions. These runs was token in the middle of the RunII, thus the features of the standard beam don't change much.

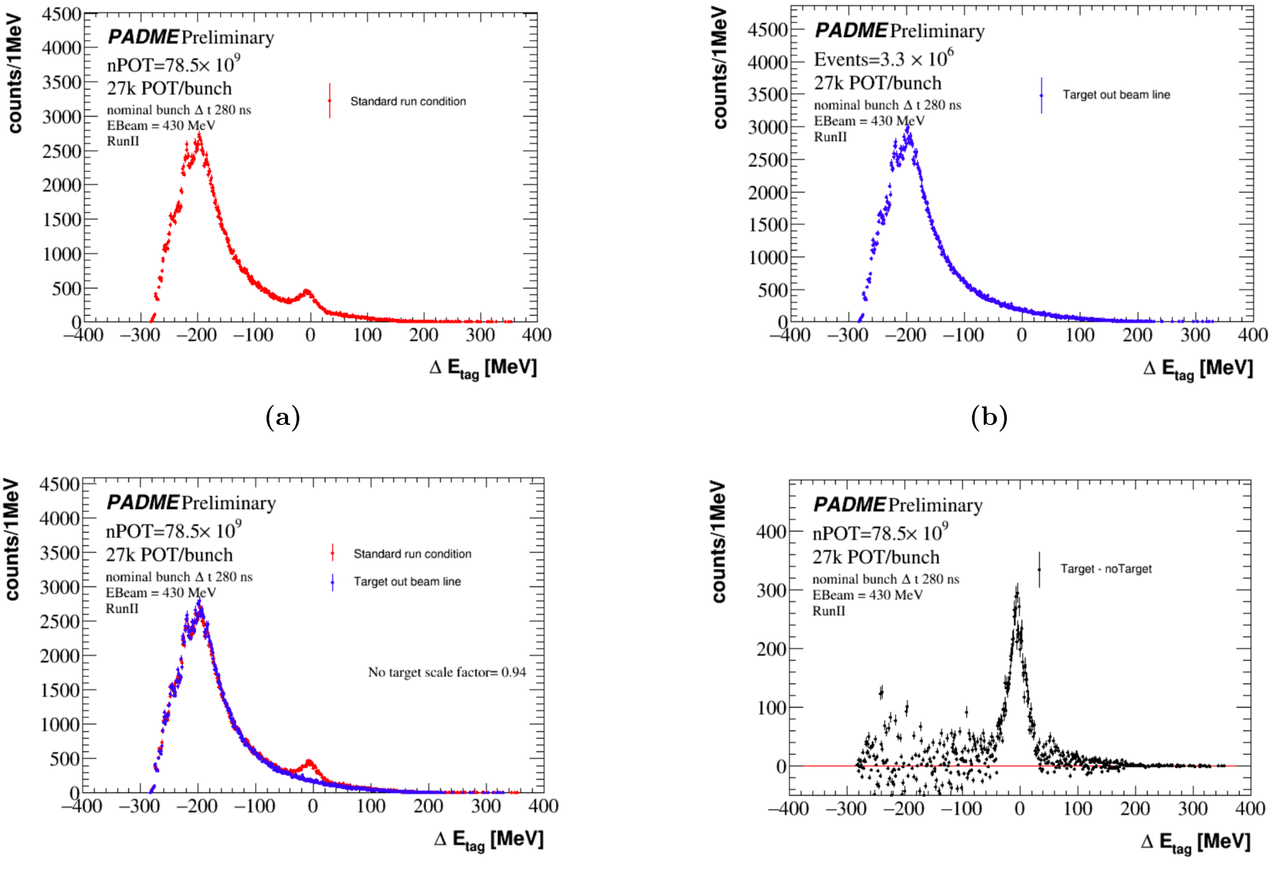

(a) (b) (c) (d)

Figure 1.27: *(a): Distribution of the* $\Delta E = E_{cl} - f(\theta)$ *of the tag distribution in a standard run condition. (b): Distribution of the* $\Delta E = E_{cl} - f(\theta)$ *for background, distribution of the events token with the target out of the beam line. (c): Comparison of (a) and scaled (b). (d) : Tag yield, obtained from the subtraction of the background on the signal.*

1.8.1 Tag and probe on data sample

The extraction of the tag and probe efficiency for the data sample procedure is the same that is described in the previous sections. The main difference with the calchep simulation is the presence of a huge background in the tag distribution. Thus the number of tag is give by the signal subtracted of the background:

$$N_{Tag}^{sig} = N_{Tag} - N_{Tag}^{bkg}. \tag{1.18}$$

The prediction of the background is made normalising the distribution obtained analysing the special runs with the target out of the beam line in the range $\Delta E_{Tag} \in [-150, -90]$ MeV.

In Figure 1.27 (a) is shown the distribution of the ΔE_{Tag} for the data sample use, in (b) is represented the background for the same distribution. A comparison of the tag distribution and the normalised background is in (c), thus its subtraction on the standard distribution in

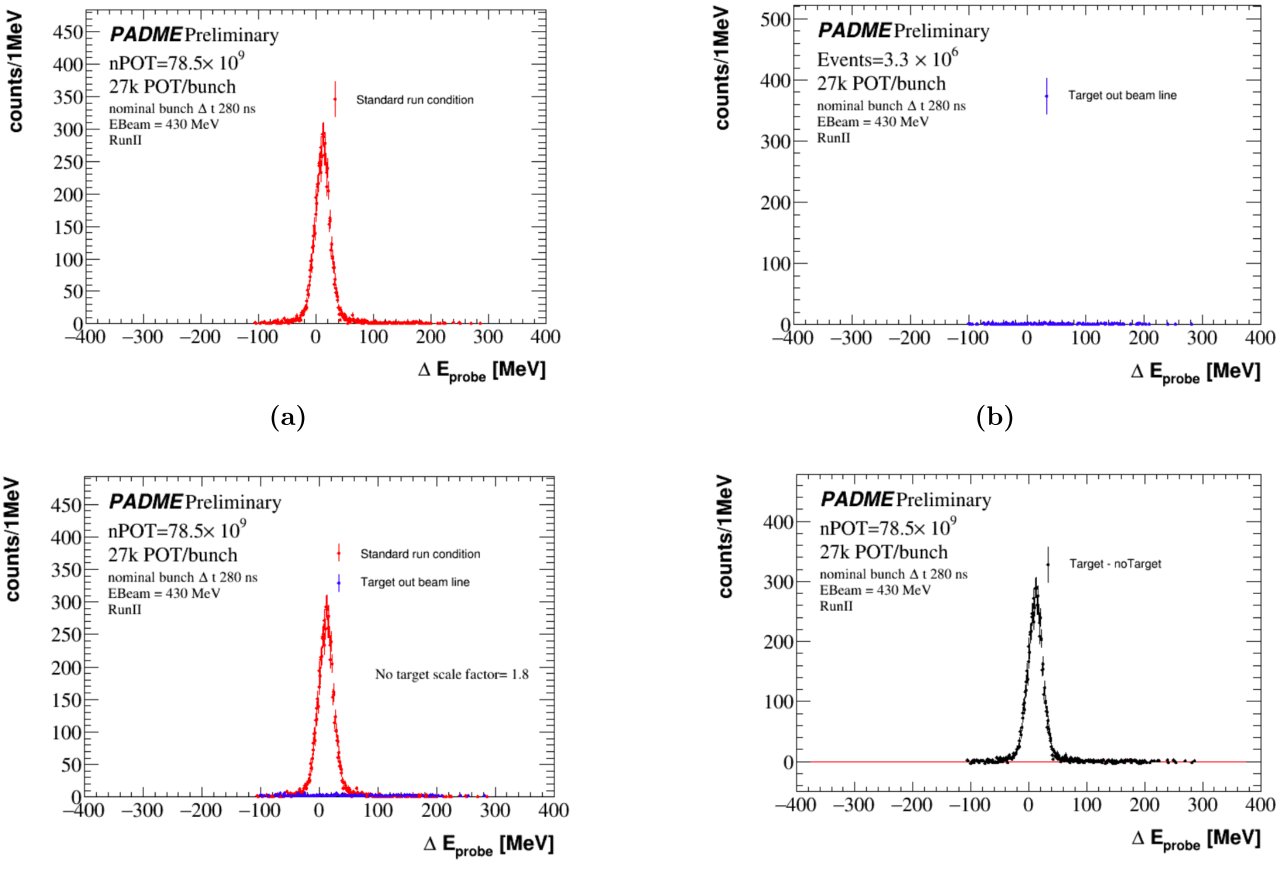

(a) (b)

(c) (d)

Figure 1.28: *(a): Distribution of the $\Delta E_{Probe} = E_{cl} - (E_{Beam} - f(\theta_{Tag}))$ of the probe matched distribution in a standard run condition. (b): Distribution of the ΔE_{Probe} for background, distribution of the events token with the target out of the beam line. (c): Comparison of (a) and scaled (b). (d) : Probe yield, obtained from the subtraction of the background on the signal.*

(c). The yield of tag is extracted integrating the distribution in $k\sigma$, where $k = 1, 3, 5$. The distribution of the probe, shown in Figure 1.28 (a), is background free (b), however in Figure (c) is reported the signal and the normalised background, in (d) the signal subtracted of the background.

The number of tags (probe) obtained is:

$$N_{tag(probe)} = (N_{inRangeTarget} - N_{inRangeNoTarget} \times f) \pm \sqrt{N^2_{inRangeTarget} + N^2_{inRangeNoTarget} \times f^2} \tag{1.19}$$

where $N_{inRangeTarget}$ is the number of events under the peak in the integrated range in the spectrum obtained analysing the runs token with a standard run condition, while $N_{inRangeNoTarget} \times f$ is the one extracted form background runs normalised with f scale factor.

1.8.2 Efficiency distribution

The efficiency is defined as:

$$\epsilon = \frac{N_{sig}^{probe}}{N_{sig}^{tag}} \pm \sqrt{\frac{\sigma_{probe}^2}{(N_{sig}^{tag})^2} + (\frac{N_{sig}^{probe}}{(N_{sig}^{tag})^2})^2 \times \sigma_{tag}^2}. \tag{1.20}$$

and is represented in Figure 1.29: (a) representation of the efficiency and the efficiency times the visible acceptance ϵ' for each bin of ECAL , (b) schematic view of the data efficiency. From the main features of the detector and the background occupancy described in Chapter data, it is expected that the inner range bins should have an higher efficiency since there is no detector problems, with the exception of bins $\phi \in [0, 45[$ Deg and $\phi \in [315, 360[$ Deg where a huge background reach ECAL . In addition the bins with $\phi \in [270, 315[$ Deg and $\phi \in [315, 360[$ Deg share a dead crystal. Regarding the outer efficiencies of upper and lower ECAL region, it is expected to observe a reduction of the efficiency due to the shadow, also with a different effect as the upper part is less affected. In addition the efficiency in bins with $\phi \in [270, 315[$ Deg and $\phi \in [315, 360[$ Deg have efficiency invalidated by the presence of a dead crystal for each bin.

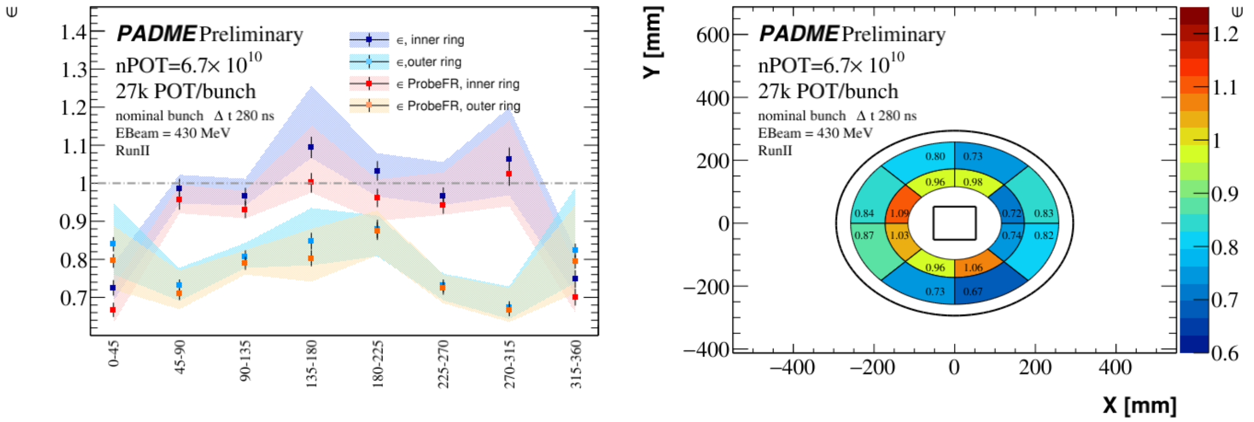

(a) (b)

Figure 1.29: *(a): Trend of the efficiency for bins in the inner ring in blue and outer once in light blue; in addition is reported the efficiency time the visible acceptance extracted requiring the probe in the FR (red for inner ring bins and orange for outer ring bins); (b) schematic view of the measured efficiency.* *eps ProbeFR -> eps'*

1.8.3 Early results

The cross section measurement was performed with both the analysis: the most energetic photon in FR and both in FR, applying the selection a.c. of Section 1.4. The N_{sig} is extracted integrating the $E_{\gamma_1} + E_{\gamma_2}$ sum of the two photons energy distribution for events that pass the annihilation selection for data subtracted of the normalised beam background obtained with the no target runs. The cross section measurement were:

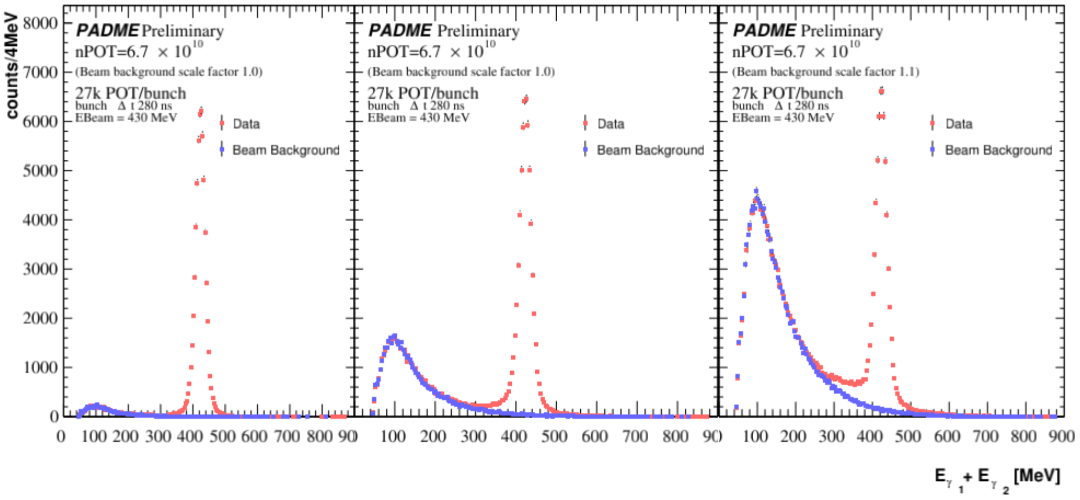

Figure 1.30: *Distribution of* $E_{\gamma_1} + E_{\gamma_2}$ *of the two photons that pass the selection a.b. described in Section 1.4 for standard run (red dots) and special one with target out of the target beam (blue dots). (a) additional selection CoG cut of* 20 mm*; (b) additional selection CoG cut of* 50 mm*; (c) additional selection CoG cut of* 80 mm.

- adding b. selection : $\sigma(e^+e^- \to \gamma\gamma) = 1.841 \pm 0.003$ mb;
- adding b.d. selections: $\sigma(e^+e^- \to \gamma\gamma) = 1.817 \pm 0.003$ mb;

with an extraction of the signal to this value, systematic errors should be added for:

- yield Tag:
    - integration of the tag and probe signals in $1, 3, 5\sigma$, quoted $+10\% - 14\%$ of the cross section measurements for both the analysis;
    - different normalisation range for the no target sample (default integration range $[-150, -90]$ MeV), quoted $+14\% - 13\%$ of the cross section measurements for both the analysis.
- Annihilation yield:
    - systematic due to the 5 cm cut on CoG distribution. In Figure 1.30 is reported the distribution of the sum of the two photons energy passing different CoG cut: $2, 5, 8$ cm. As is visible from the distribution the beam related background approximated using the no target special run, and normalising the two distribution in the range $[0, 200]$ MeV, is not able to reproduce the signal background with the choose of a larger CoG cut. Using these three points a systematic was extracted and quoted $+11\% - 10\%$;

- systematic due to the integration of the signal in different $E_{\gamma_1} + E_{\gamma_2}$ ranges (default integration range $[300, 700]$ MeV), it is extracted changing the normalisation range and is quoted $+4\% - 1\%$ of the cross section measurement for both the analysis.

The high systematics on the measurements is mainly due to the high uncertainty on the tag signal, thus a hard work was done and reported to reduce all these systematics.

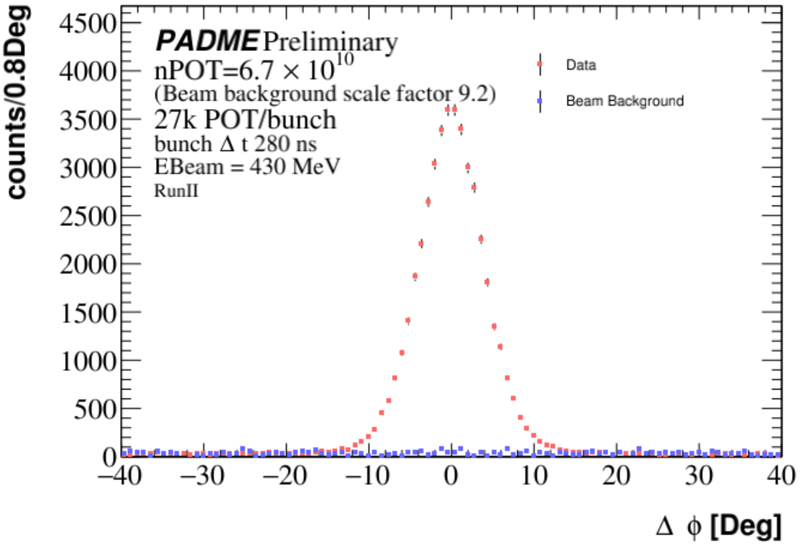

Figure 1.31: *Distribution of* $\Delta\phi = \phi_{\gamma_1} - \phi_{\gamma_2} - 180$ Deg *of the two photons that pass the selection a.b.c. described in Section 1.4 for standard run (red dots) and special one with target out of the target beam (blue dots).*

Since there is agreement in the analyses performed with the most energetic photon in FR and both the photons in FR, and since it is proved that the ϵ' measured with both the photons in FR is given by the product of the efficiency and the visible acceptance, the following study was done only requiring the most energetic photon belonging FR.

1.9 Event selection and Results

1.9.1 Pre-selection

A first screening of the events was done in order to chose only events where a beam bunch arrives in the experiment, this is possible by choosing event triggered by the hardware trigger of the BTF beam.

However, even when the PADME trigger board receives the BFT trigger signal, it can happen that the event is empty, typically because of a late update of the BFT trigger signal after beam loss.

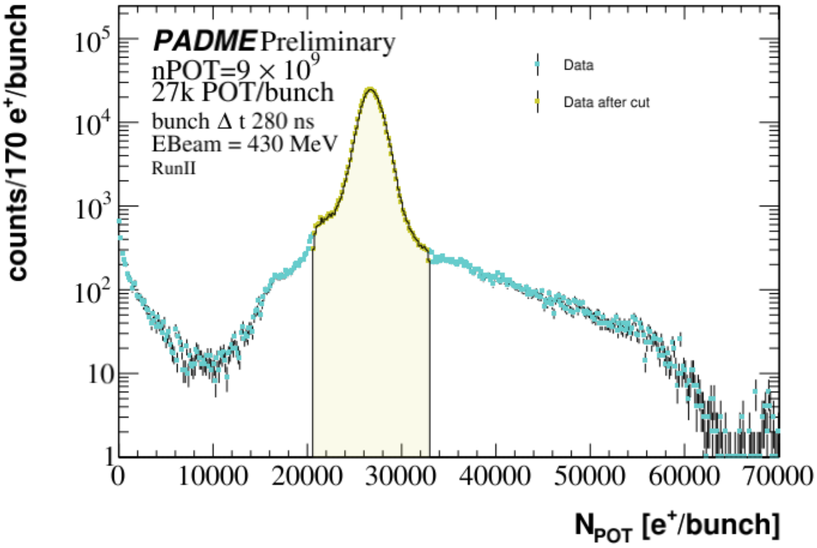

Figure 1.32: *Distribution of the Number of Positrons On Target per bunch for run* $N = 30563$ *(azure distribution). In yellow is reported the* N_{POT}*/bunch distribution of the events that pass the multiplicity selection.*

In addition, another problem can be observed looking at Figure 1.32 where the N_{POT} distribution for the events triggered by the BTF signal is shown for run $N = 30563$. Up to 70 kPOT/bunch were estimated in a few cases. To solve both these problems in each run, events with a measured number of positrons in the bunch above or below five sigma from the average bunch multiplicity have been discarded. The reason of this cut lie the fact that if the target is reconstructing correctly the bunch multiplicity, events out the 5σ have a different beam background level and are affected by the pileup differently with respect to a typical event. On the other hand, instead events where the signals readout from the strips of the Diamond target lead to an extremely low or unrealistically high measurement of the total charge lead to a wrong assessment of the number of positrons in the bunch. Although the occurrence of such events is low, they may introduce biases in the measurement of the total number of positrons on target.

In Table 1.16 the number of events for each runs before and after the luminosity selection are reported along with the fraction of events retained.

1.9.2 Photon pre-selection

In Chapter data taking) it has been shown that even in RunII the PADME electromagnetic calorimeter receives a high rate of background particles, from beam related spurious interactions. Most of the times the resulting energy deposits have low energy, therefore the features of the corresponding clusters are statistically different from those of photons of energy above about 90 MeV that, as we will see later, are involved with the annihilation process. Therefore a cluster selection is applied in order to reduce the contamination of the cluster collection and

Table 1.16: *For each run analysed the number of events triggered by the BTF trigger signal, the number of events passing the luminosity selection and their ratio are reported.*

Run number	N_{ev}^{BTF}	$N_{ev}^{5\sigma}$	$\frac{N_{ev}^{5\sigma}}{N_{ev}}$
30369	2961470	2820916	$0,953$
30386	1437248	1307072	$0,909$
30547	2232745	2140028	$0,958$
30553	785728	746250	$0,95$
30563	2243220	2101791	$0,937$
30617	2206172	2086402	$0,946$
30624	2234949	2106551	$0,943$
All	14000000	13300000	$0,95$

improve the rejection of background.

Cluster quality requirements

Several features of the clusters corresponding to a tight selection of annihilation events have been studied and contrasted with the same quantities observed in the overall sample of clusters. The selection of annihilation photon candidates was based in the following requirements: at least two clusters must be found in ECAL with $|t_{\gamma_1} - t_{\gamma_2}| < 10$ ns, $|\Delta\phi| = |\phi_{\gamma_1} + 180° - \phi_{\gamma_2}| < 25°$, $|CoG_{X(Y)}| < 5$ cm, $300 < E_{\gamma_1} + E_{\gamma_2} < 500$ MeV [5]. In addition the most energetic cluster in the pair was requested to be at a radial distance with respect to the direction of the incoming beam bigger than 115.82 mm.

The distributions (with arbitrary relative normalization) of the variables studied are reported in Figure 1.33 for all clusters (azure distribution) and for annihilation candidate pho-

Table 1.17: *Cluster quality requirements and fraction of clusters passing each cut with respect to those passing the previous cut.*

Quality cut	$\frac{N_i}{N_{i-1}}$
$R_{Cl-seed} < 20$ mm	0.96
$X_{RMS} \geq 1$ mm	0.79
$Y_{RMS} \geq 1$ mm	0.90
$\Delta X^{max} \geq 1$ mm	1.
$\Delta Y^{max} \geq 1$ mm	1.
$\lvert lcc \rvert \leq 0.99$ mm	0.92
t_{RMS}	0.996
Isolation	0.85

---

[5] The definition of x, y_{CoG} and the motivations of these cuts will be explained in Section 1.4

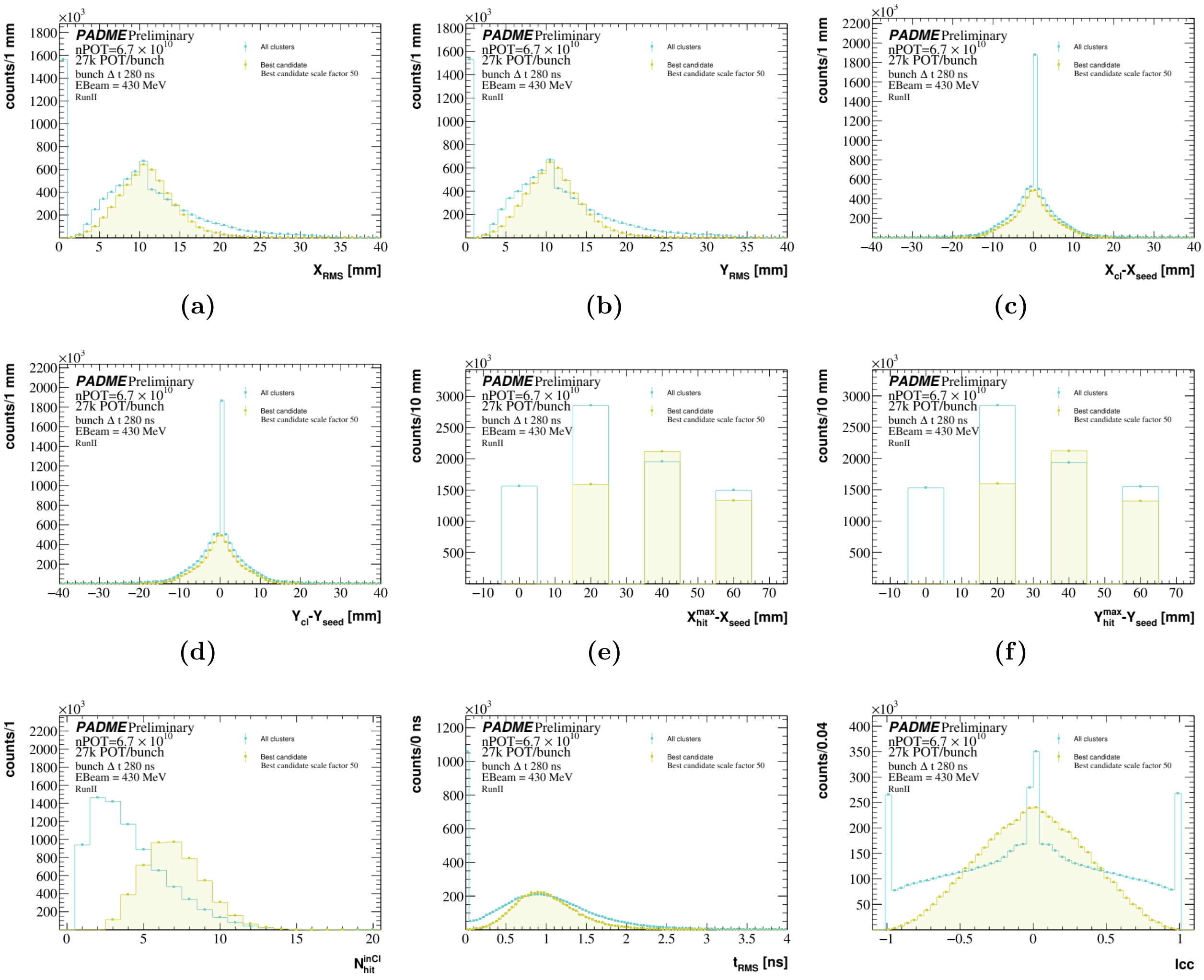

(a) (b) (c)

(d) (e) (f)

(g) (h) (i)

Figure 1.33: *Cluster features, used to improve the quality and reduce the background contamination of the cluster sample, for all clusters (azure distributions) and annihilation candidate photons (yellow distribution): (a) RMS of X coordinates for hits in cluster, (b) RMS of Y coordinates for hits in cluster, (c) distance of cluster position from its seed in the X and Y (d) direction (e) maximum distance between a hit in the cluster and the seed in the X and Y (f) direction, (g) cluster size, (h) time RMS, (i) linear correlation coefficient of hits in the cluster.*

tons. For each variable, a loose cleanup cut was defined to avoid compromising significantly the efficiency for signal photon. In the following the relevance of each variable is briefly described:

- the distance between the cluster position and its seed is peaked at zero in both the X and Y directions (see Figure 1.33 (c) and (d)), large distances may only be due to anomalous situations related for example by pileup; therefore only clusters with $R_{cl-seed} =$

$(X_{Cl} - X_{seed})^2 + (Y_{Cl} - Y_{seed})^2 < 20$ mm are retained;

- X and Y RMS, defined as

$$\sqrt{\frac{\sum_{i=0}^{n_{hit \in Cl}} (X(Y)_i - X(Y)_{Cl})^2 E_i}{\sum_{i=0}^{n_{hit \in Cl}} E_i}}, \tag{1.21}$$

  are shown in Figure 1.33 (a) for X and (b) for Y RMS. A comparison between generic clusters and annihilation candidates suggest to reject clusters with $X(Y)_{RMS} \leq 1$ mm;

- the maximum distance between hits in a cluster and the cluster position along X and Y axis (Figure 1.33 (e) and (f)) is requested to be $\Delta X(Y)^{max} \geq 1$ mm in order to discard the occurrence of signals from noise in an isolated crystal;

- the cluster distribution size, reported in Figure 1.33 (g), shows that candidate photons have an average multiplicity of 7 hits per cluster, thus a threshold was defined $N_{hits}^{inCL} > 1$;

- the RMS of the time distribution of hits in a cluster, defined similarly to the X(Y) RMS, is shown in Figure 1.33 (h) and a value not exceeding 3 ns is requested;

- the linear correlation coefficient of hits in the cluster given by

$$lcc = \frac{\sum_{i=0}^{n_{hit}} (X_i - Xcl)(Y_i - Ycl) E_i}{\sum_{i=0}^{n_{hit}} E_i \times X_{RMS} \times Y_{RMS}} \tag{1.22}$$

  is reported in Figure 1.33 (i); only values below 0.99 are accepted;

- finally an isolation requirement is applied: a photon is rejected if another cluster in a time within 10 ns is found closer than 200 mm.

The sequence of cuts applied to the ECAL clusters rejects 53, 8% of them with the relative efficiency cut flow reported in Table 1.17. The fraction of the signal rejected is the 10% given by (number of probe that pass NPotSelection and ClQuality / number of probe that pass only NPOTSelection)/2 - I divided for 2 to consider also the number of tag, since I select a probe if I found the tag....How I can explain this now?.

1.9.3 Choice of the event selection requirements

In order to correct the annihilation yield with the efficiency extracted form tag and probe technique, the same preliminary selection that it is applied in the searching of the matched probe was applied to the photon: $E_\gamma > 90$ MeV and $|\Delta E| = |E_\gamma - E(\theta_g)| < 100$ MeV.

As discussed the extraction of the two photons annihilation yield measurement is characterised by a not negligible systematic, this is due to the technique used in the extraction of the signal (integration of the signal subtracted of the background in a fixed range) and on the selection that is used to identify the annihilation events. In order to erase the systematic due the CoG cut, the selection used for the following analysis is just the a. and b. cuts described in Section 1.4. Aiming to reduce the systematic due to the yield extraction other variables was studied. In particular it is searched a variable with a flat background, as can be the $\Delta t = t_{\gamma_1} - t_{\gamma_2}$, but as is shown in Figureput reference Chapter data taking Figure Dt, the beam related background has a bump at zero. For this reason and since the annihilation has a constrained kinematic, the variable $\Delta\phi = \phi_{\gamma_1} - \phi_{\gamma_2} - 180°$ is studied. As is represented in Figure 1.31 the beam related background has a flat distribution in $\Delta\phi$. In addition, to be coherent with the efficiency measurement, to each photon is required to pass an annihilation pre-selection: $E_\gamma > 90$ MeV and $|\Delta E| = |E_\gamma - f(\theta_g)| < 100$ MeV. The two photons annihilation yield extraction is consequentially done fitting the $\Delta\phi$ with a background and signal function represented by a polynomial of second degree and a gaussian. Then using the background prediction function the yield is extracted as:

$$N_{Sig} = N_{ev} - N_{Bkg}^{fit}. \tag{1.23}$$

A data-driven geometry correction

In order to verify the consistency of the annihilation, the ECAL calorimeter is divided in 8 azimuthal angle slices. In Table 1.18 are reported the yields of the annihilation for each bin, where the belonging to the bin is defined by the bin of the most energetic photon. The run analysed is the numbered 30563.

Table 1.18: *Annihilation yields measured fitting the background of the $\Delta\phi$ distribution for each azimuthal ECAL bin and the relative ratio of the yields with to respect the higher one.*

ϕ Deg **range**	N_{sig}	$\frac{N_{sig}}{N_{sig}^{max}}$
$[0, 45]$	1227	0.85
$[45, 90]$	899	0.62
$[90, 135]$	866	0.60
$[135, 180]$	1316	0.91
$[180, 225]$	1451	1
$[225, 270]$	1290	0.90
$[270, 315]$	1091	0.75
$[315, 360]$	1334	0.92

Apparently the annihilation center seems shifted towards negative x and y coordinates. This is in agreement with the measurement done in a survay, where emerges that the ECAL center is located in $(x_c, y_c) = (-3.13, -3.86)$ mm in the PADME framework. In addition the run took in account has a global Center Of Gravity shifted with to respect the zero of PADME , in fact a fit on the gaussian peak over the background shown a spatial centroid in $CoG = (X_{CoG}, Y_{CoG}) = (0.86, 0.67)$ mm. The annihilation axis is then shifted in order to be the same of the PADME one. The position of all the photons were shifted of:

$$X_\gamma = X_\gamma^{PADME} + X_c - X_{CoG}. \tag{1.24}$$

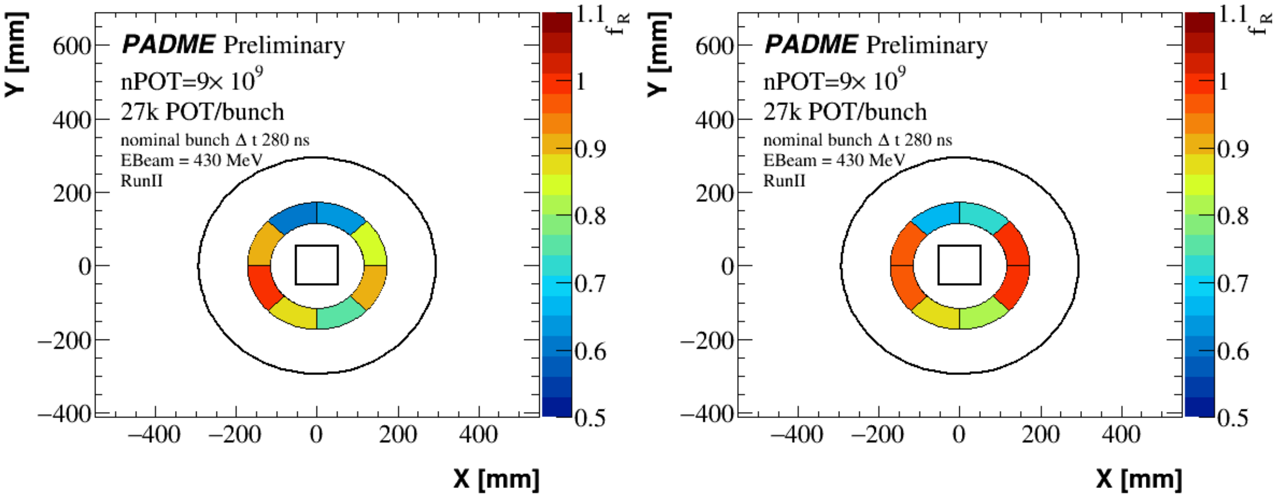

(a)

(b)

Figure 1.34: *(a) Schematic view of the ratio between the bin maximum annihilation yield and the signals observed in each bin f_R. The belonging to this latest is defined by the most energetic photon. (b) f_R observed after the cluster position correction.*

After the alignment of the detector with the annihilation physic the so obtained annihilation yields are reported in Table 1.19 divided in azimuthal slices (bin belonging is defined by the bin of the most energetic photon). In Figure 1.34 are shown the ratio between the maximum yield measured in the ECAL bins and the yields of each azimuthal slice for (a) clusters not shifted, (b) adding the shift of Equation 1.24. As is visible after the correction the yields are consistent with the ECAL features, in fact along the x axis, where there are not detector problem, the ratio of the yields are uniform. The bins along the y axis have a low yield with to respect

Table 1.19: *Annihilation yields after the cluster position correction measured fitting the background of the $\Delta\phi$ distribution for each azimuthal ECAL bin and the relative ratio of the yields with to respect the higher one.*

ϕ Deg **range**	N_{sig}	$\frac{N_{sig}}{N_{sig}^{max}}$
$[0, 45]$	1352	1
$[45, 90]$	966	0.71
$[90, 135]$	901	0.67
$[135, 180]$	1295	0.96
$[180, 225]$	1294	0.96
$[225, 270]$	1182	0.87
$[270, 315]$	1089	0.81
$[315, 360]$	1332	0.99

the other bins, and this is due to the shadow of the magnet, and since this effect is different between the top and the bottom of ECAL , the yields are different between the two ECAL regions. In addition a difference due to the dead crystals is observed.

1.9.4 Improving on tag modelling

The major problem in the tag yield extraction is the modelling of the background. A cleaning of the background was done with the pre-selection. The reduction of background in the tag samples in shown in Figure 1.35 where are reported the distribution of ΔE_{tag} identified tag belonging the fiducial region without any selection in blue, for the events that pass the nPOT selection in grey and in red the events that pass the nPOT selection and photons that pass the cluster quality one.

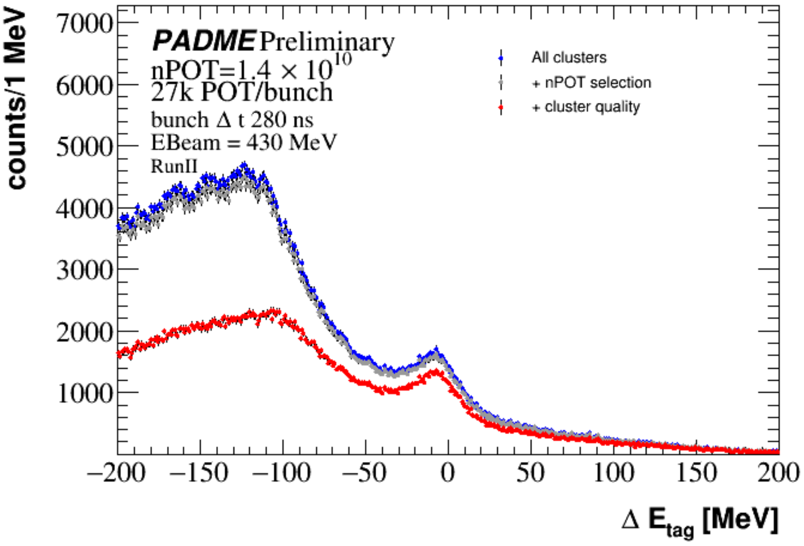

Figure 1.35: ΔE_{Tag} *distribution of r identified tag belonging the fiducial region in blue. The same distribution is reported in grey for events that pass the nPOT selection and in red the photons that pass also the cluster quality cuts.*

The main contribution to the background in data sample comes from the beam related background and the pileup one. The first one, as specified before, is predicted by the no target run, instead the simulation of pure annihilation in a bunch of $25000e^+$ is used to predict the pileup background. From the total spectrum of ΔE_{tag}, the annihilation peak was removed and the empty region was fit with a exponential added to a polynomial of one degree function. Once obtained the function $f(\Delta E^i_{Tag})$. In Figure 1.39 is reported an example of pileup background used for the tag yield extraction for photons with $R \in [172.82, 258[$ mm and $\phi \in [180, 225[$ Deg.

Consequentially the fit of the tag distribution was performed fitting the ΔE_{Tag} spectrum in the range $[-100, 100]$ MeV fitted using for the description of the background the two samples just described and for the signal two gaussian function. In Figure **??** (a) is shown an example of

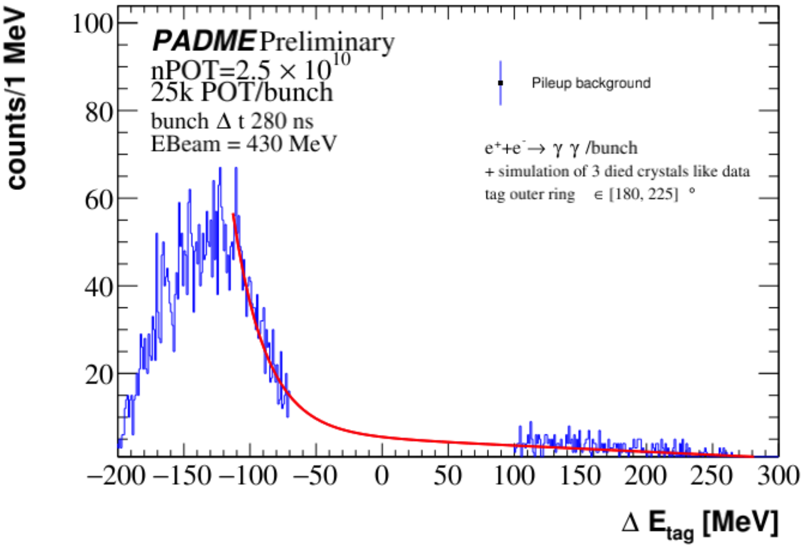

Figure 1.36: *Distribution of pileup background in the tag distribution extracted using MC simulation of one annihilation events generated by CalcHEP and predict the signal region fitting with an exponential and polynomial of one order degree functions.*

fit made for the tag belonging the inner ring of ECAL and with $\phi \in [180, 225[$ Deg, (b) example of fit made for the tag belonging the outer ring of ECAL and with $\phi \in [45, 90[$ Deg . The first was optimised using RooFit add reference, that allow to use the background distributions as probability function. The fit from which the signal was extracted is the one with the function parameters set have the minimum in the Negative Logarithmic Likelihood and of the error on the signal.

In the plot are reported all the contributions on data represented with the black dot: the red solid line represent the total fit, the orange line represent the total signal, given by the sum of the two gaussian component (yellows distributions). The total background prediction is reported in cyan, that is given by the sum of beam background (blue) and the pileup one (green). The fit parameters are 7: fraction of the total signal over the total background $f_{s/b}$, the fraction of the pileup over the beam related background, the faction of a gaussin over the total signal, mean and sigma of the two gaussian functions. From the fraction $f_{s/b}$ it is possible the extraction of the tag yield:

$$N_{tag} = f_{s/b} \times N \pm \sqrt{(f_{s/b} \times \sqrt{N})^2 + (N \times \Delta f_{s/b})^2} \tag{1.25}$$

where N is the total number of events in the fit range and $\Delta f_{s/b}$ is the error on the fraction extracted from fit. The estimation of the yield using this technique, integrating in a large range, fix the bias observed integrating in the 3σ, thus the $\epsilon(R_\gamma, \theta_g)$ represent a photon efficiency.

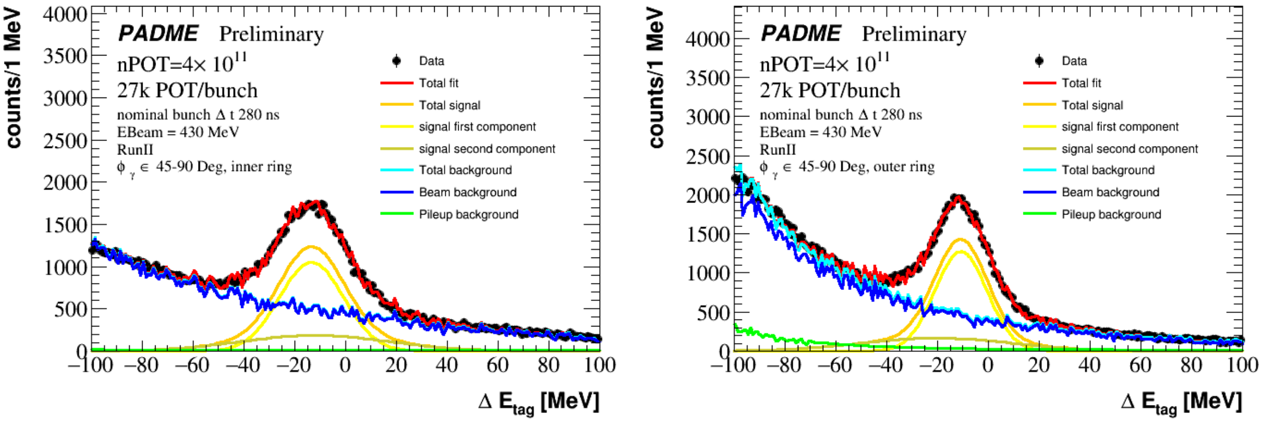

(a) **(b)**

Figure 1.37: *Fit of the* ΔE_{Tag} *distribution for photon belonging (a)* $R \in]115.8, 172.82[$ mm *and* $\phi \in [180, 225[$ Deg*, (b)* $R \in [172.82, 258[$ mm *and* $\phi \in [45, 90[$ Deg*. The data (black dots) is fitted with a total function (red line) given by the sum of a total signal component in orange (composed by two gaussian function in yellow) and a total background component in cyan (given by the sum of pileup effect in green and the beam related background in blue).*

1.10 Cross section measurement after multiplicity selection

Using the modelling of the distribution ΔE_{Tag} described in Section 1.9.4 and applying the multiplicity selection, the efficiency was extracted as:

$$\epsilon = \left[\frac{N^{3\sigma}_{probe}}{N^{RF}_{tag}}\right]_{N_{POT} selection} \tag{1.26}$$

where the tag yields were extracted fitting with RooFit and the probe yields form the integration in 3σ in the ΔE_{probe} distribution. The efficiency measured is reported in Table 1.20 for each of the eight phi bins with probe belonging the inner ring and the eight phi bins with the probe in the outer ring. The efficiency trend is also shown in Figure 1.38 (a), a schematic view in Figure 1.38 (b).

From the cross section definition reported in Equation 1.1, multiplying it for a factor $g = 8$ to obtain the total cross section, the cross sections for each bins were extracted. For the measurement it is used:

- $N_{POT} = 3.97 \times 10^{11}$ extracted using the corrected target calibration maybe it is needed a section where is described the changes in me nPOT measurement. NB: all the previous plots and estimations were done with the first approximation of nPOT.;

- $Acc = 0.0634$ extracted using the NLO Babayaga sample for a positron energy of $E_{e^+} =$ 430 MeV;

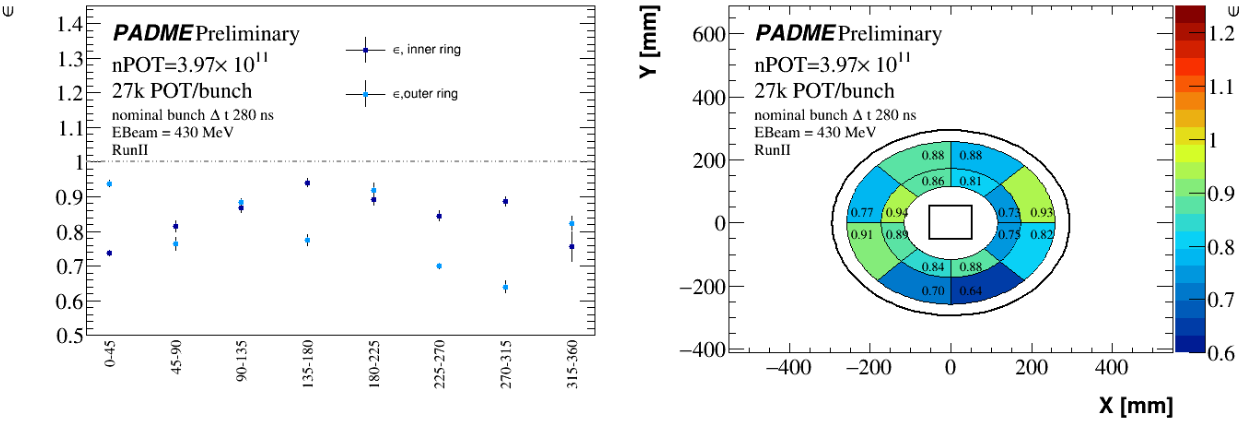

(a) (b)

Figure 1.38: *(a): Trend of the efficiency for bins in the inner ring in blue and outer once in light blue obtained requiring the multiplicity selection; (b) schematic view of the measured efficiency.*

Table 1.20: *Number of tag yield* N_{Tag} *and its error* ΔN_{Tag}*, number of probe* N_{Probe} *with the error* ΔN_{Probe} *and the efficiency* ϵ *measured form the ratio of the probe over the tag yield with the error* $\Delta\epsilon$ *obtained applying the propagation of the tag and probe errors. The yields are obtained with events that pass the multiplicity selection.*

ϕ [Deg]	N_{Tag}	ΔN_{Tag}	N_{Probe}	ΔN_{Probe}	ϵ	$\Delta\epsilon$
			Inner ring			
$[0, 45]$	62318	648	45968	214	$0,738$	$0,008$
$[45, 90]$	42433	816	34575	186	$0,815$	$0,016$
$[90, 135]$	37141	545	32266	180	$0,869$	$0,014$
$[135, 180]$	47867	580	45034	212	$0,941$	$0,012$
$[180, 225]$	53620	910	47780	219	$0,891$	$0,016$
$[225, 270]$	50830	813	42960	207	$0,845$	$0,014$
$[270, 315]$	46465	617	41207	203	$0,887$	$0,013$
$[315, 360]$	57955	337	43815	209	$0,756$	$0,006$
			Outer ring			
$[0, 45]$	48803	481	45787	214	$0,938$	$0,01$
$[45, 90]$	56531	1400	43167	208	$0,764$	$0,019$
$[90, 135]$	46797	457	41402	203	$0,885$	$0,01$
$[135, 180]$	57192	1084	44342	211	$0,775$	$0,015$
$[180, 225]$	51248	1078	47112	217	$0,919$	$0,02$
$[225, 270]$	51337	530	35982	190	$0,701$	$0,008$
$[270, 315]$	53048	1416	33954	184	$0,640$	$0,017$
$[315, 360]$	55798	1253	45976	214	$0,824$	$0,019$

- ϵ: each yield is corrected using the efficiency of the bins where the photons falls, the values used are reported in Table 1.20.

The measurement was done using the two photons yield obtained fitting the distribution of $\Delta\phi$ for events that has two photons passing the annihilation pre-selection, time coincidence of 10 ns request and having the most energetic photon in the FR. As cross check of the cross section measurement is also extracted using the yields of the single photon obtained form the ΔE_{Tag} distributions (photons are corrected with the efficiency of the belonging bin) for the inner ring and outer one. The cross sections obtained are reported in Table 1.21. A trend of them as a function of the phi slice is reported in Figure 1.39, where the measurement obtained with two photons and a single photon is reported: in violet is reported the measurement obtained with the two photons yield extracted with the $\Delta\phi$ distribution, in orange it is reported the measurement obtained with the tag yields for the inner ring and in azure the cross section obtained form the tag yields belonging the outer ring and sorting them as a function of the most energetic photon phi (the photon in $[0, 45]$ Deg and outer ring has the most energetic photon in the inner ring of $[180, 225]$ Deg, thus it is allocated to this latest bin. This is done to observe coherent cross sections).

Table 1.21: *Cross sections measured with the yields of one (Tag in the inner ring and Tag in the outer ring) and two photons as a function of them azimuthal angles.The cross sections are obtained with events that pass the multiplicity selection.*

ϕ [Deg]	$\sigma_{\Delta\phi}$ [mb]	σ_{TagIn} [mb]	σ_{TagOut} [mb]
$[0, 45]$	$2,127 \pm 0,051$	$2,104 \pm 0,05$	$1,732 \pm 0,035$
$[45, 90]$	$1,843 \pm 0,043$	$1,908 \pm 0,042$	$2,015 \pm 0,06$
$[90, 135]$	$1,76 \pm 0,055$	$1,849 \pm 0,058$	$1,59 \pm 0,028$
$[135, 180]$	$1,73 \pm 0,045$	$1,796 \pm 0,046$	$2,265 \pm 0,046$
$[180, 225]$	$1,707 \pm 0,036$	$1,659 \pm 0,034$	$2,054 \pm 0,05$
$[225, 270]$	$2,051 \pm 0,061$	$2,027 \pm 0,06$	$1,834 \pm 0,041$
$[270, 315]$	$1,65 \pm 0,033$	$1,598 \pm 0,028$	$1,758 \pm 0,053$
$[315, 360]$	$2,3 \pm 0,048$	$2,292 \pm 0,047$	$1,76 \pm 0,046$

1.11 Results

1.11.1 Phi dependence

Another cross section measurement was done for events that pass the multiplicity selection and photons that pass the cluster quality cuts. A preliminary step is to measure the selection efficiency, thus for each of 16 bins was measured the efficiency as:

$$\epsilon = \left[\frac{N^{3\sigma}_{Probe}}{N^{RF}_{Tag}}\right]_{N_{POT} slectionandclusterquality} \tag{1.27}$$

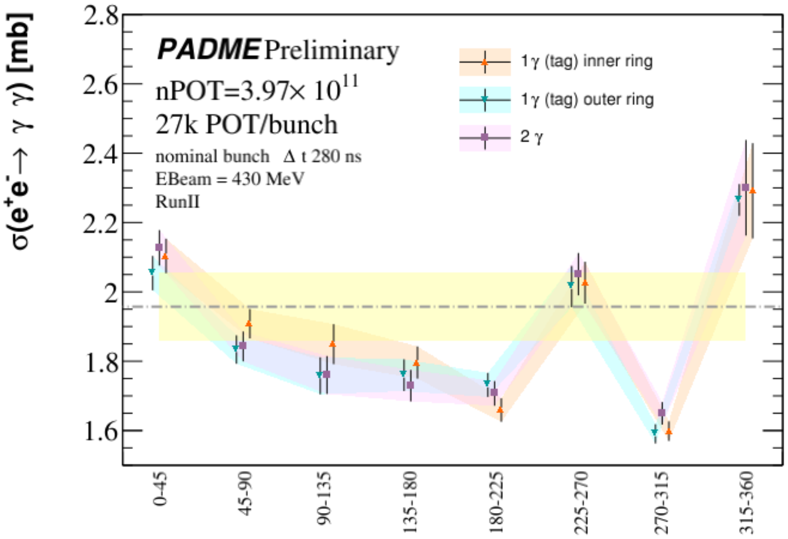

Figure 1.39: *Trend of the cross section as a function of the phi slice (the annihilation photon belong to a phi bin if the respective most energetic photon belong to that bin). The yellow strip represent the uncertainty of* 5% *on the multiplicity measurement. The orange dots are the cross section measurement done with a single photon obtained from tag yields in the inner ring, the azure one is the cross section trend obtained from the single photon from tags in the outer rings, the violet are the cross sections obtained with the two photons (selection: annihilation pre-selection, most energetic photon in FR and time coincidence of* 10 ns*).*

where the $N^{3\sigma}_{Probe}$ correspond to the matched probe yield obtained integrating ΔE_{Probe} in 3σ from the mean value and N^{RF}_{Tag} is the tag yield obtained fitting the ΔE_{tag} with RooFit.

The yields and the corresponding efficiencies is reported in Table 1.22 for each phi slice, both inner and outer ring. In Figure 1.40 (a) is shown the trend efficiency as a function of the azimuthal angle for the inner and outer ring of ECAL , in figure 1.40 (b) a schematic view of them. As is visible the efficiency is lower than the one obtained with only the multiplicity selection, but it appear as more stable. For this selection the cross section for the single photon was extracted also fitting the missing mass squared, in fact the M^2_{miss} variable (it will be used to verify the existence of the dark photon) return, in case of annihilation photon, a value equal to 0 MeV. In Figure 1.41 the missing mass squared for photons with $R \in [115.8, 172.82[$ mm and $\phi \in [45, 90[$ Deg is shown. Superimposed to the data reported with the back dots, there is the total fit in red, composed by the background contribution in cyan (pileup effect in green summed with the beam related background in blue) and the signal contribution in orange (two yellows gaussian contributions). As for the tag, the single photon yield is given by the sum of the two gaussian functions. The two photons annihilation yield and consequentially cross section with ΔE_{tag} and M^2_{miss} for inner and outer ring is measured to check the yields consistency along with the efficiency measured. In fact the four distribution, although they are composed by the same events in same phi and radius bin, they have a different representation of the background. In Figure 1.42 there is the comparison between the (a) ΔE_{tag} and (b) M^2_{miss} distributions

Table 1.22: *Number of tag yield N_{Tag} and its error ΔN_{Tag}, number of probe N_{Probe} with the error ΔN_{Probe} and the efficiency ϵ measured form the ratio of the probe over the tag yield with the error $\Delta\epsilon$ obtained applying the propagation of the tag and probe errors. The yields are obtained with events that pass the multiplicity selection and photons that pass the cluster quality cuts.*

ϕ [Deg]	N_{Tag}	ΔN_{Tag}	N_{Probe}	ΔN_{Probe}	ϵ	$\Delta\epsilon$
			Inner ring			
$[0, 45]$	51972	1076	37459	194	0,721	0,015
$[45, 90]$	38315	575	28423	169	0,742	0,012
$[90, 135]$	32427	372	26629	163	0,821	0,011
$[135, 180]$	50356	1659	36394	191	0,723	0,024
$[180, 225]$	56982	1273	38890	197	0,682	0,016
$[225, 270]$	45297	470	35562	189	0,785	0,009
$[270, 315]$	46322	803	33608	183	0,726	0,013
$[315, 360]$	51591	819	35279	189	0,684	0,011
			Outer ring			
$[0, 45]$	44848	868	37872	195	0,844	0,017
$[45, 90]$	47468	732	35524	188	0,748	0,012
$[90, 135]$	45301	778	33984	184	0,75	0,014
$[135, 180]$	45687	837	35608	189	0,779	0,015
$[180, 225]$	46946	759	38162	195	0,813	0,014
$[225, 270]$	46732	520	29428	172	0,63	0,008
$[270, 315]$	53746	1421	27660	166	0,515	0,014
$[315, 360]$	45774	439	36687	192	0,801	0,009

between the inner ring in blue and outer one in pink for photons with $R \in]115.8, 172.82[$ mm and $\phi \in [180, 225[$ Deg. As is shown the two distributions of both the variables have different modelling of background and also of the signal. As described in previous section, the yields of two photons and from single photon were corrected with the efficiency $\epsilon(R, \phi)$ and the cross section was extracted as a function of the azimuthal angle dividing them for the other constants. The measurements are reported in Table 1.23 for all the annihilation: two photons yield from the $\Delta\phi$ distribution and the single photon yield from tag and missing mass squared in both inner and outer ring. All the measurements were plotted as a function of the azimuthal bin in Figure 1.43, where the two photon cross section measurement is reported in violet (selection: most energetic photon in FR and time coincidence of 10 ns), the single photon in: orange for tag in the inner ring, azure for tag in the outer ring, missing mass yield in pink for inner ring and green for outer ring.

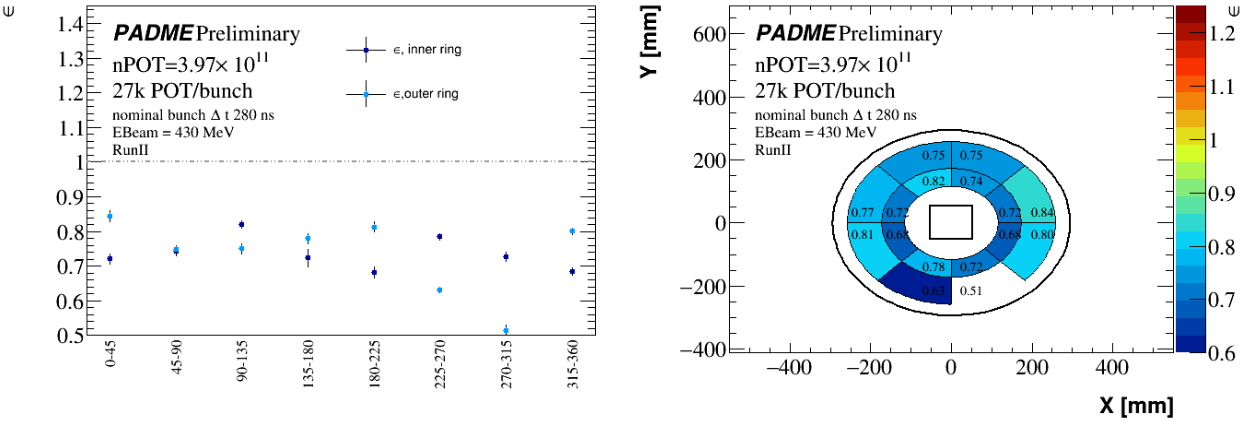

(a)

(b)

Figure 1.40: *(a): Trend of the efficiency for bins in the inner ring in blue and outer once in light blue obtained requiring the multiplicity selection and cluster quality cuts; (b) schematic view of the measured efficiency.*

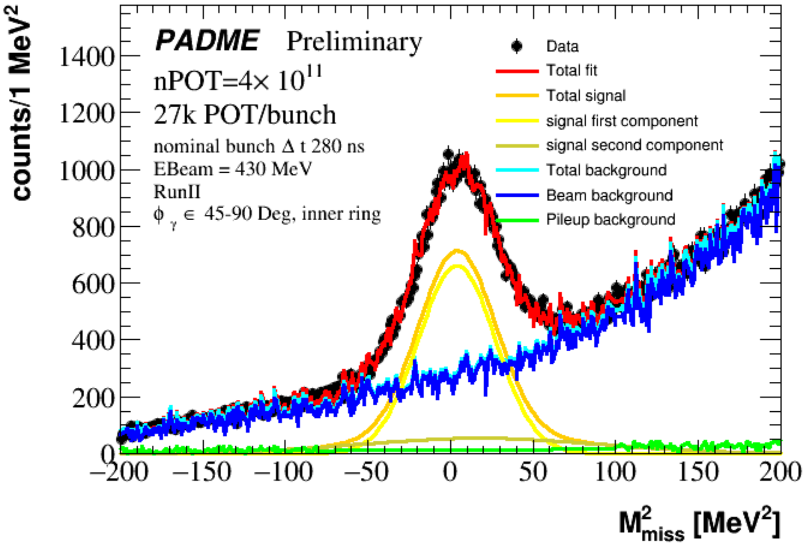

Figure 1.41: *Fit of the missing mass squared distribution for photon belonging* $R \in]115.8, 172.82[$ mm *and* $\phi \in [45, 90[$ Deg. *The data (black dots) is fitted with a total function (red line) given by the sum of a total signal component in orange (composed by two gaussian function in yellow) and a total background component in cyan (given by the sum of pileup effect in green and the beam related background in blue.*

1.11.2 Run dependence

To study the stability of the result as a function of the pileup, beam background and beam structure, the cross section was extracted as a function of the run: for each run it was extracted a global efficiency for the inner ring and a global efficiency for the outer one. In Table 1.24

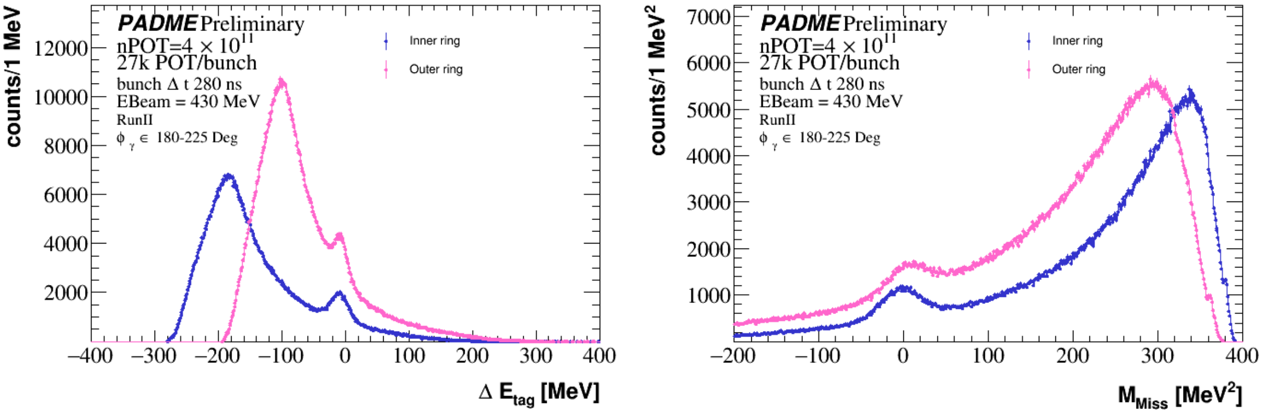

(a) (b)

Figure 1.42: *Comparison between the (a) ΔE_{tag} and (b) M^2_{miss} in inner (blue dots) and outer (pink dots) ring belonging. The variables are extracted from photons with $R \in]115.8, 172.82[$ mm and $\phi \in [180, 225[$ Deg.*

Table 1.23: *Cross sections measured with the yields of one (Tag and missing mass squared in the inner ring and Tag and missing mass squared in the outer ring) and two photons as a function of them azimuthal angles. The cross sections are obtained with events that pass the multiplicity selection and photons that pass the cluster quality cuts.*

ϕ [Deg]	$\sigma_{\Delta\phi}$ [mb]	$\sigma_{\Delta E_{In}}$ [mb]	$\sigma_{\Delta E_{Out}}$ [mb]	$\sigma_{MM^2_{In}}$ [mb]	$\sigma_{MM^2_{Out}}$ [mb]
$[0, 45]$	$2,005 \pm 0,056$	$1,972 \pm 0,052$	$2,045 \pm 0,062$	$1,971 \pm 0,056$	$2,067 \pm 0,048$
$[45, 90]$	$1,856 \pm 0,041$	$1,908 \pm 0,037$	$1,834 \pm 0,035$	$1,989 \pm 0,035$	$1,865 \pm 0,037$
$[90, 135]$	$1,899 \pm 0,06$	$1,983 \pm 0,059$	$1,871 \pm 0,048$	$1,846 \pm 0,042$	$1,889 \pm 0,039$
$[135, 180]$	$1,959 \pm 0,068$	$1,918 \pm 0,066$	$2,006 \pm 0,05$	$2,025 \pm 0,069$	$2,056 \pm 0,043$
$[180, 225]$	$2,039 \pm 0,065$	$1,992 \pm 0,061$	$1,936 \pm 0,052$	$2,103 \pm 0,052$	$1,862 \pm 0,045$
$[225, 270]$	$1,873 \pm 0,04$	$1,832 \pm 0,035$	$1,842 \pm 0,036$	$1,814 \pm 0,053$	$1,892 \pm 0,031$
$[270, 315]$	$1,964 \pm 0,052$	$1,89 \pm 0,047$	$1,907 \pm 0,056$	$1,836 \pm 0,038$	$1,927 \pm 0,055$
$[315, 360]$	$2,05 \pm 0,051$	$2,023 \pm 0,049$	$1,904 \pm 0,066$	$2,056 \pm 0,084$	$1,741 \pm 0,033$

are reported the tag and probe yields and the efficiency $\epsilon(R)$ for each run used. An efficiency trend is also reported in Figure 1.44 for a global inner ring efficiency in blue and a global outer efficiency in light blue. The latest point of the trend correspond to the whole statistic, where it is extracted a global efficiency as a function of the photon radius. Having the efficiency for each run, the cross section can be obtained correcting for the beam condition. As before, the yield measured were the one of the two photon annihilation and the other one related to the single photon annihilation. For this latest measurement the tag yields were used. This time the cross sections were extracted using for each run its number of POT and in the total cross section it is not included the factor $g = 8$ that it is used for the cross section as a function of

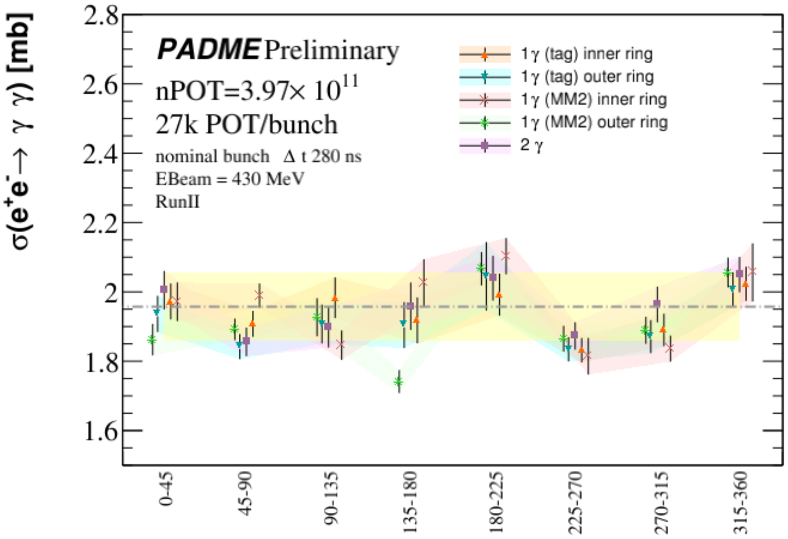

Figure 1.43: *Trend of the cross section as a function of the phi slice (the annihilation photon belong to a phi bin if the respective most energetic photon belong to that bin). The yellow strip represent the uncertainty of* 5% *on the multiplicity measurement. The orange dots are the cross section measurement done with a single photon obtained from tag yields in the inner ring, the azure one is the cross section trend obtained from the single photon form tags in the outer rings, the pink dots correspond to the cross section obtained from the missing mass squared of photons in the inner ring, the green are from photons measured from missing mass squared spectrum for clusters in outer ring and the violet are the cross sections obtained with the two photons (selection: most energetic photon in FR and time coincidence of* 10 ns*).*

phi. The resulted measurement were summarised in Table 1.25 and represented in Figure 1.45.

1.11.3 Systematics

The central value of the annihilation in two photons cross section is defined to be the one measured using the two photons selection, since the $\delta\phi$ has a flat background, thus less subjected to background modelling errors, all phi slices together, fitting all the statistic and using the average efficiency. The measurement is $\sigma(e^+e^-\to\gamma\gamma) = 1,973 \pm 0,030$ mb, where the error is due to the statistical error on yield and to statistical error on efficiency.

The systematic error due to the efficiency determination on detector defects and uneven background distribution in ECAL is extracted from the stability of the two photons cross section in phi slices, and extracted measuring the RMS of all the measurements weighted with the errors, thus once estimated the weighted cross section mean as $\sigma_\mu = \frac{\sum \sigma_i/\Delta\sigma_i^2}{1/\Delta\sigma_i^2}$, the RMS is extracted as:

$$\sqrt{\frac{\sum((\sigma_i - \sigma_\mu)/\Delta\sigma_i)^2}{\sum 1/(\Delta\sigma_i)^2}} \tag{1.28}$$

Table 1.24: *Number of tag yield N_{Tag} and its error ΔN_{Tag}, number of probe N_{Probe} with the error ΔN_{Probe} and the efficiency ϵ measured form the ratio of the probe over the tag yield with the error $\Delta\epsilon$ obtained applying the propagation of the tag and probe errors. as a function of the run. The yields are obtained with events that pass the multiplicity selection and photons that pass the cluster quality cuts.*

Run number	N_{Tag}	ΔN_{Tag}	N_{Probe}	ΔN_{Probe}	ϵ	$\Delta\epsilon$
			Inner ring			
30369	71134	1678	52342	229	0,736	0,018
30386	26007	437	20540	143	0,790	0,014
30547	66487	928	49152	222	0,739	0,011
30553	25134	1966	18106	135	0,720	0,057
30563	55459	3493	40371	201	0,728	0,046
30617	56665	4407	41912	205	0,740	0,058
30624	61268	3005	44042	210	0,719	0,035
All runs	36000	4252	267373	517	0,743	0,009
			Outer ring			
30369	74918	1106	52684	230	0,703	0,011
30386	27854	1038	20631	144	0,741	0,028
30547	67095	1839	49476	222	0,737	0,02
30553	26343	877	18171	135	0,690	0,024
30563	56505	1356	40587	201	0,718	0,018
30617	57951	1830	41805	204	0,721	0,023
30624	63696	1425	44355	211	0,696	0,016
All runs	37562	2951	268098	518	0,714	0,006

Table 1.25: *Cross sections measured with the yields of one (Tag in the inner ring and Tag in the outer ring) and two photons as a function of run number.The cross sections are obtained with events that pass the multiplicity selection and cluster quality cuts.*

Run number	$\sigma_{\Delta\phi}$ [mb]	$\sigma_{\Delta E_{In}}$ [mb]	$\sigma_{\Delta E_{Out}}$ [mb]
30369	$1,941 \pm 0,057$	$1,872 \pm 0,053$	$1,861 \pm 0,053$
30386	$1,98 \pm 0,082$	$1,904 \pm 0,079$	$1,896 \pm 0,078$
30547	$1,988 \pm 0,063$	$1,911 \pm 0,06$	$1,899 \pm 0,058$
30553	$2,051 \pm 0,178$	$1,959 \pm 0,168$	$1,95 \pm 0,167$
30563	$2,012 \pm 0,139$	$1,936 \pm 0,131$	$1,926 \pm 0,131$
30617	$1,989 \pm 0,168$	$1,92 \pm 0,162$	$1,927 \pm 0,162$
30624	$2,07 \pm 0,112$	$2,006 \pm 0,107$	$1,993 \pm 0,108$
All runs	$1,973 \pm 0,03$	$1,914 \pm 0,028$	$1,909 \pm 0,028$

where $\Delta\sigma$ is the error on the cross section. The resulting systematic error is 0.073 mb.

The systematic error due to the background conditions is measured from the stability of the

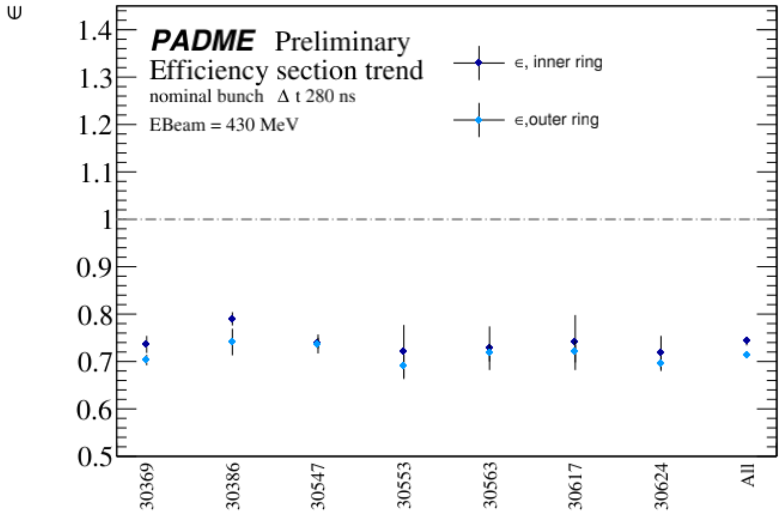

Figure 1.44: *Trend of the efficiency for inner ring in blue and outer one in light blue obtained requiring the multiplicity selection and cluster quality cuts extracted for each run. The last point represent the global efficiency of the whole data taking*

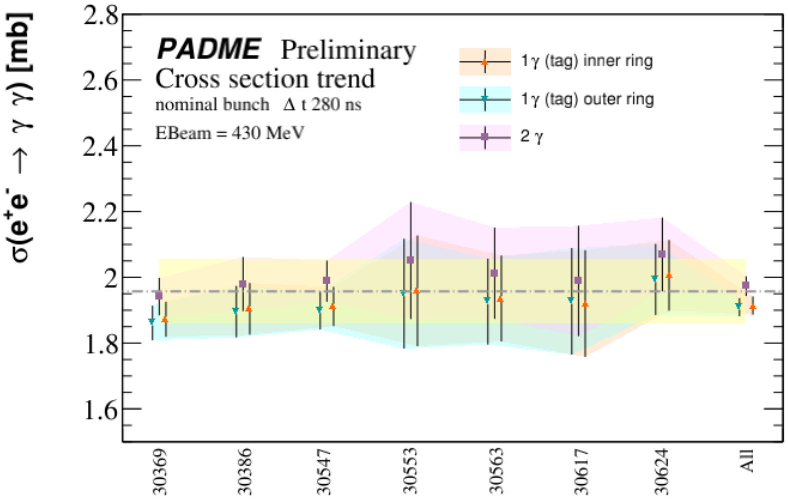

Figure 1.45: *Trend of the cross section as a function of the run. The yellow strip represent the uncertainty of* 5% *on the multiplicity measurement. The orange dots are the cross section measurement done with a single photon obtained from tag yields in the inner ring, the azure one is the cross section trend obtained from the single photon form tags in the outer rings, the violet are the cross sections obtained with the two photons (selection: most energetic photon in FR and time coincidence of* 10 ns*).*

cross section as a function of the run. Also for this systematic the average cross section was extracted as $\sigma_\mu = \frac{\sum \sigma_i/\Delta\sigma_i^2}{1/\Delta\sigma_i^2}$ and then measured the weighted RMS as:

$$\sqrt{\frac{\sum((\sigma_i - \sigma_\mu)/\Delta\sigma_i)^2}{\sum 1/(\Delta\sigma_i)^2}} \tag{1.29}$$

obtaining a systematic error of 0.0382 mb.

Another systematic error can be introduced in order to took into account the calorimeter granularity and of the definition of the minimum and maximum radii of the fiducial region: this can be extracted using the cross section extracted with single photon yield in the inner and outer ring of ECAL : $1.914 - 1.909 = 0,005$ mb.

The systematic errors due to the acceptance can come from the theoretical error, that since the measurement was done at NLO was negligible, and from the dependency on the knowledge of the distance between ECAL and target, that as discussed in Section put ref is negligible. Another systematic can be due to the energy scale, but introducing a variation of the energy scale of $\pm 0,3\%$ the acceptance change of $< 0,1\%$, thus also this can be negligible.

The total systematic error due to the sum of the defect and background correction (phi stability), background and pileup condition (run stability) and ECAL granularity and FR assumption (comparison ΔE_{In} and ΔE_{Out}) is $0.073 + 0.038 + 0.005 = 0,082$ mb.

An additional systematic error is due to the N_{POT} measurement, and it is quoted to be of the 5%.

The final measurement is:

$$\sigma(e^+e^- \to \gamma\gamma) = 1,973 \pm 0,030\ (\text{stat}) \pm 0,082\ (\text{syst}) \pm 0,098\ (\text{lumi})\ \text{mb} \tag{1.30}$$

that is compatible with the measurement of Babayaga at NLO $\sigma = 1.9573 \pm 0.0051$ mb (for reference Babayaga estimation at LO is $\sigma = 1.9110 \pm 0.0004$ mb).

Bibliography

[1] F. Oliva, The padme active diamond target and positron bremsstrahlung analysis (2021).

[2] M.Raggi, et al., Performance of the padme calorimeter prototype at the daϕne btf, Nuclear Instruments and Methods in Physics Research A (862) (2017) 31–35.

[3] CAEN. [link].
URL `https://www.caen.it/products/v1742/`

[4] PSI. [link].
URL `https://www.psi.ch/drs/DocumentationEN/DRS4rev09.pdf`